Journal of the European Ceramic Society 46 (2026) 117860

Contents lists available at ScienceDirect

Journal of the European Ceramic Society

journal homepage: www.elsevier.com/locate/jeurceramsoc

Constitutive modeling of pressure-assisted powder consolidation by spark plasma sintering: The case of transition metal diborides

Gabriele Traversari, Mariano Casu, Luca Cappai, Giorgio Carta, Michele Brun, Alberto Cincotti, Roberto Orrù, Giacomo Cao, Antonio Mario Locci *

Università degli Studi di Cagliari, Dipartimento di Ingegneria Meccanica, Chimica e dei Materiali, Via Marengo 3, Cagliari 09123, Italy

ARTICLE INFO

Keywords:
Refractory borides
Pressure-assisted sintering
Modeling
Powder rheology

ABSTRACT

A viscoplastic constitutive model is developed to describe the pressure-assisted consolidation of HfB_2, NbB_2, and TiB_2 powders by spark plasma sintering (SPS). Densification is modeled as the superposition of two mechanisms: particle rearrangement at low temperature, represented by a rate-independent plastic slider, and high-temperature viscous flow, described by a dashpot following a Bird–Carreau law. These elements act in series, enabling a smooth transition from plastic to viscous behavior as temperature, porosity, and strain rate evolve. Model thermodynamic consistency is demonstrated by deriving the stress–strain rate law from a dissipation potential and linking it to the plastic yield function. Porosity evolution is described by coupling mass and momentum balance equations, and model parameters (viscosities, activation energy, strain-rate sensitivity) are identified by fitting experimental porosity–time data. The model is validated against literature data and used to identify the most effective operating conditions for achieving full densification of refractory diborides.

1. Introduction

Transition metal diborides (TMBs), such as HfB_2, NbB_2, and TiB_2, are among the most promising candidates for high-temperature structural applications in the aerospace sector due to their exceptional thermal stability, high melting points (>3000 °C), and excellent hardness and good oxidation resistance [1–3]. These ultra-high-temperature ceramics (UHTCs) are particularly attractive for components operating in extreme aerothermal environments, such as sharp leading edges, thermal protection systems, and propulsion-facing parts of hypersonic vehicles [4,5]. However, their practical application remains limited by the intrinsic difficulty of densifying these materials to near-theoretical densities without sintering additives, which can compromise the desired high-temperature performances [6].

Spark plasma sintering (SPS) has emerged as a key processing route to address this challenge, enabling rapid densification through the simultaneous application of uniaxial pressure and pulsed direct electric current [7–10]. While many experimental efforts have demonstrated enhanced consolidation of TMBs using SPS, understanding of the densification mechanisms of these materials under pressure-assisted conditions and the corresponding modeling approaches remain incomplete.

Several attempts have been developed in the literature to describe the kinetics of pressure-assisted sintering. Pioneering continuum-scale models, notably those by Olevsky and co-workers [11,12], treat SPS as a thermomechanical process, incorporating aspects of temperature distribution, pressure, and macroscopic densification. Based on this approach, further refinements have been proposed to improve the mathematical description of the densification process occurring during SPS [13–16]. While these models have contributed significantly to the simulation of SPS for oxide and metallic systems, they generally neither address the densification behavior of TMBs, nor account for the microstructural mechanisms unique to such ceramics, especially early-stage particle rearrangement underload, which plays a critical role in densification kinetics but is often neglected.

Additionally, most models of pressure-assisted techniques adopt a power-law creep description, or the densification rate is related to applied stress and temperature through semi-empirical or phenomenological expressions [17,18]. Although this approach can describe the main features of viscous deformation for some materials, it lacks the flexibility to represent transitions between distinct consolidation mechanisms and imposes assumptions regarding the rheological behavior that may not hold true across materials or processing windows. Moreover, few studies explicitly incorporate particle rearrangement as a separate mechanism, an omission that becomes critical for

* Corresponding author.
E-mail address: antoniom.locci@unica.it (A.M. Locci).

https://doi.org/10.1016/j.jeurceramsoc.2025.117860
Received 5 August 2025; Received in revised form 11 September 2025; Accepted 29 September 2025
Available online 30 September 2025

Notation

Latin letters

A	empirical coefficient depending on ρ, [-]
A_T	midpoint inflection temperature for σ_Y, [K]
a^0	pre-exponential factor, [Pa s]
B	empirical coefficient depending on ρ, [-]
B_T	steepness of the sigmoidal function for σ_Y, [K]
F	yield function, [Pa]
$f(\theta)$	porosity dependence function for equivalent strain rate, [s^{-1}]
$\overrightarrow{g}$	gravity field, [m s^{-2}]
HR	heating rate, [K s^{-1}, °C s^{-1}]
I_1	the first invariant of the Cauchy stress tensor, [Pa]
J_2	second invariant of the deviatoric Cauchy stress tensor, [Pa]
m	strain-rate sensitivity coefficient, [-]
p	contact pressure exerted by the sample to the die internal wall, [Pa]
Q_η	activation energy, [J mol^{-1}]
r	radial coordinate, [m]
$\mathbf{T}$	total stress tensor, [Pa]
T	temperature, [K, °C]
T_D	dwell temperature, [K, °C]
t	time, [s]
t_D	dwell period length, [s]
t_H	heating period length, [s]
$tr(\ )$	trace of a tensor, [-]
$\overrightarrow{v}$	velocity field, [m s^{-1}]
W	equivalent strain rate, [s^{-1}]
$\overrightarrow{x}$	spatial coordinates vector, [m]

Greek letters

$\dot{\gamma}$	second invariant of the strain rate tensor deviator $\boldsymbol{\varepsilon}'$, [-]
δ_{ij}	Kronecker delta dunction, [-]
$\boldsymbol{\varepsilon}$	strain tensor, [-]
$\dot{\boldsymbol{\varepsilon}}$	strain rate tensor, [s^{-1}]
$\dot{\varepsilon}_{ij}$	strain rate tensor component, [s^{-1}]
$\dot{\boldsymbol{\varepsilon}}'$	strain rate deviator tensor, [s^{-1}]
$\dot{\varepsilon}'_{ij}$	strain rate tensor deviatoric component, [s^{-1}]
η	shear viscosity, [Pa s]
η^*	shear viscosity of the dense (pore-free) material, [Pa s]
η^0	zero-shear rate viscosity of dense (pore-free) material, [Pa s]
ϑ	hoop coordinate, [rad]
θ	porosity, [-]
Λ	plastic multiplier, [-]
κ	bulk viscosity, [Pa s]
κ^*	shear viscosity of the dense (pore-free) material, [Pa s]
λ	material-specific relaxation time, [s]
λ^0	pre-exponential factor, [s K $^{\left(\frac{m-1}{m}\right)}$]
μ	apparent viscosity, [Pa s]
ρ	relative density, [-]
$\boldsymbol{\Sigma}$	Σ tensor defined for shorter notation, [Pa]
Σ_{ij}	component of the Σ tensor, [Pa]
$\boldsymbol{\sigma}$	Cauchy stress tensor, [Pa]
σ_{app}	applied stress, due to mechanical load, [Pa]
σ_{eq}	equivalent stress, [Pa]
σ_{ij}	Cauchy stress tensor component, [Pa]
σ'_{ij}	Cauchy stress tensor deviatoric component, [Pa]
σ_Y	yield strength, [Pa]
σ_Y^0	low temperature asymptotic value for σ_Y, [Pa]
σ_Y^∞	high temperature asymptotic value for σ_Y, [Pa]
Φ	dissipation potential, [Pa s]
φ	function of sample porosity for shear viscosity, [-]
Ψ	viscoplastic potential, [Pa]
Ψ^P	plastic potential, [Pa]
ψ	function of sample porosity for bulk viscosity, [-]

Superscripts

^{P}	referred to plastic deformation
^{VP}	referred to visco-plastic deformation
^{0}	referred to t = 0

Subscripts

$_1$	referred to the Body/Element 1
$_2$	referred to the Body/Element 2
$_r$	referred to the r coordinate
$_z$	referred to the z coordinate
$_\alpha$	referred to the generical α coordinate
$_\vartheta$	referred to the ϑ coordinate

high-hardness materials like TMBs, where this phenomenon precedes or takes place simultaneously with the viscous deformation [19].

In this work, a generalized rheological model that describes the dual-mechanism nature of SPS densification in TMBs is proposed. The model conceptualizes the consolidation process as the serial coupling of two rate-controlling elements: a slider representing the rate-independent particle rearrangement at lower temperatures, and a slider and dashpot in parallel ensemble that describes the nonlinear viscous flow at elevated temperatures. This framework allows the model to naturally simulate the transition between the two mechanisms as a function of temperature, porosity, and strain rate.

Therefore, unlike traditional creep-based models, the proposed approach avoids *a priori* assumption about the densifying powder behavior. The strain-rate sensitivity is indeed an output of the fitting process, thus enabling the model to flexibly represent both linear (Newtonian) and nonlinear (shear-thinning) regimes depending on the intrinsic properties of the material and the applied conditions. Furthermore, the proposed model is shown to be thermodynamically consistent. Indeed, the stress–strain rate relationship of the viscous component is derived from a dissipation potential, and it is demonstrated that the adopted yield function of the sliders can be rigorously derived from the dual viscoplastic potential. In this way, the present work provides a thermodynamically consistent framework capable of unifying different densification mechanisms within a single formulation, thus offering a novel tool for reliably simulating the pressure-assisted consolidation of transition metal diborides.

Rheological parameters, including viscosities, pre-exponential factors, activation energies, and strain-rate sensitivities, are obtained through least-squares fitting of porosity–time curves from SPS experiments on HfB_2, NbB_2, and TiB_2. These ceramics, in addition to being among the individual metal diborides mostly investigated from the experimental viewpoint, are also frequently involved as constituents of high-entropy borides, which have recently attracted significant interest. It is also shown that accounting for early-stage particle rearrangement is essential for correctly identifying viscosity parameters; neglecting this mechanism systematically leads to underestimated values of, for instance, activation energies. Model results are validated against density data from the literature and used to identify the influence of operating conditions for achieving full densification in each material. This work introduces a physically grounded, generalizable modeling framework

for pressure-assisted sintering of ultra-high-temperature ceramics with direct implications for designing advanced aerospace components based on TMBs.

2. Mathematical model

Spark plasma sintering of transition metal diborides is modelled in this work by assuming that powder compaction is given by the superimposition of two different phenomena: 1) particle rearrangement of an

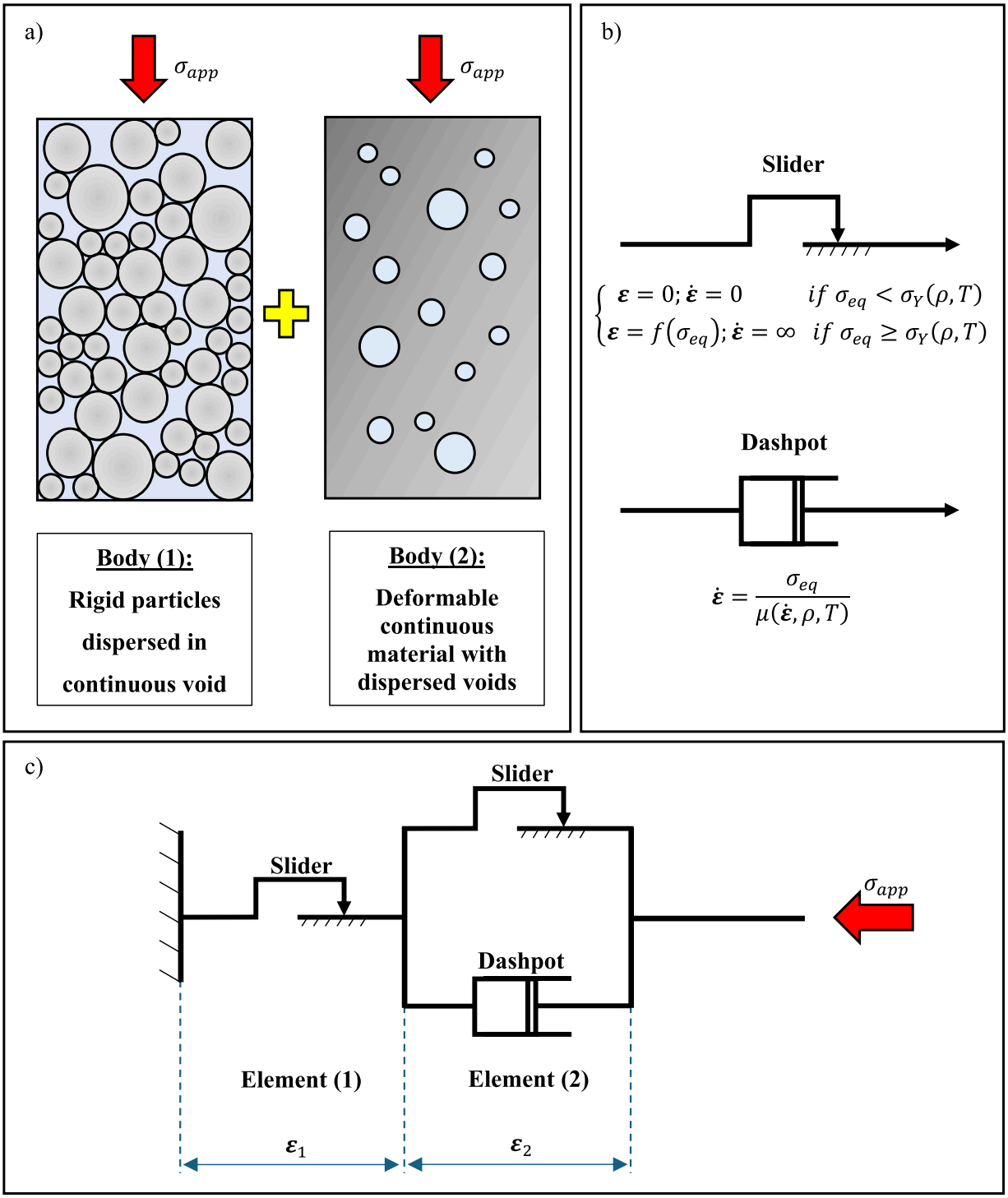

Fig. 1. Schematic representation of the two-stage viscoplastic model of densification. a) Conceptual decomposition of the powder compact into two idealized bodies: Body (1) represents the initial stage with rigid particles dispersed in a continuous void network, while Body (2) models the subsequent deformable porous medium consisting of a continuous solid matrix with voids. b) Rheological elements governing densification: the slider simulates particle rearrangement via a stress-dependent ideal plastic threshold (activated when the equivalent stress σ_{eq} exceeds the yield strength σ_Y), while the dashpot describes viscous deformation, governed by an apparent viscosity $\mu(\dot{\varepsilon}, \rho, T)$ dependent on strain rate, porosity, and temperature. c) Mechanical analog of the full model: Element (1) accounts for particle rearrangement while Element (2) reproduces the densification of the continuous porous matrix through viscous flow. The two elements act in series and are subjected to the same applied uniaxial stress σ_{app}.

ensemble of rigid (non-deformable) particles and 2) deformation of a porous continuous matrix (cf. Fig. 1). Both phenomena are caused by the application of the uniaxial load and are supposed to depend upon temperature, porosity, and strain rate levels. From a rheological perspective, particle rearrangement can be represented as an instantaneous plastic deformation of the Body (1) provided that the effective applied stress exceeds the yield strength $\sigma_{Y,1}$ that characterizes this particle ensemble. Creep (viscous sintering) is instead considered responsible for the time-dependent deformation of the continuous Body (2) whose rate depends on its apparent viscosity μ. This quantity is taken temperature, porosity, and shear rate dependent. As for the case of Body (2), it is assumed that viscous consolidation occurs if the effective applied stress is higher than the corresponding yield strength $\sigma_{Y,2}$.

It is worth noting that the present model assumes ideal boride powders, free from oxides, secondary phases, or other surface impurities that are commonly present in real powders. Moreover, other properties of the starting powder (for instance particle size and aspect ratio), which are also expected to affect its densification behavior, are not considered in this work. This simplification is adopted to isolate and characterize the intrinsic densification behavior of the boride phase. While such impurities can influence surface diffusion, particle rearrangement, and effective viscosity, their effects are beyond the scope of the current study and will be considered in future extensions of the model. Moreover, since the present work is focused on the rheological behavior of the powder, temperature was treated as an input rather than a coupled variable and it is assumed to be uniform within the sample, along with a negligible effect of the contact resistances. These features, which are known to play an important role in the SPS technology, have been already addressed in our previous work [20].

The model description depicted above can be translated to the rheological schematization shown in Fig. 1 **(panel b and c)**, where two elements in series are involved. Element 1 is given by a slider that represents the powder compaction as an effect of the re-packing of rigid particles and their mutual friction and wear. Element 2 is given by a dashpot and a slider in parallel and describes the viscoplastic densification of the porous Body (2) whose rheological equivalent is a Bingham fluid. This representation has also been named as *supple body* [21].

According to the description reported above, $\boldsymbol{\varepsilon}_1^P$ is the plastic (rate independent) strain of Element 1 and $\boldsymbol{\varepsilon}_2^{VP}$ represents the viscoplastic strain (rate dependent) of Element 2. The total strain of the sample is thus defined as follows:

$$\boldsymbol{\varepsilon} = \boldsymbol{\varepsilon}_1^P + \boldsymbol{\varepsilon}_2^{VP} \tag{1}$$

where

$$\boldsymbol{\varepsilon}_1^P = \begin{cases} 0 & if \sigma_{eq} < \sigma_{Y,1} \\ \neq 0 & if \sigma_{eq} \geq \sigma_{Y,1} \end{cases} \tag{2a}$$

$$\boldsymbol{\varepsilon}_2^{VP} = \begin{cases} 0 & if\ \sigma_{eq} < \sigma_{Y,2} \\ \neq 0 & if\ \sigma_{eq} \geq \sigma_{Y,2} \end{cases} \tag{2b}$$

The reader is referred to the Notation section for the definition of all mathematical symbols used in the text.

The total strain tensor $\boldsymbol{\varepsilon}$ determines the sample consolidation whose dynamics can be described in terms of the relative density field $\rho(\vec{x},t)$, that is given by the total mass balance (continuity) equation:

$$\frac{\partial \rho}{\partial t} + \nabla \bullet (\rho \vec{v}) = 0 \tag{3}$$

The velocity field $\vec{v}(\vec{x},t)$ appearing in Eq. (3) can be obtained by solving the linear momentum balance equation:

$$\frac{\partial}{\partial t}(\rho \vec{v}) + \nabla \bullet \mathbf{T} - \rho \vec{g} = 0 \tag{4}$$

Tensor $\mathbf{T}$ can be interpreted as the linear momentum flux and it can be split into two parts:

$$\mathbf{T} = \rho \vec{v}\,\vec{v} - \boldsymbol{\sigma} \tag{5}$$

The first term on the r.h.s. of Eq. (5) represents the convective part of the flux. Second term is the Cauchy stress tensor, which completely describes the state of stress of the compacting sample. Expression of the latter tensor depends upon the mechanical properties of the materials the system is composed of. Neglecting inertial and gravitational effects, the momentum balance Eq. (4) assumes the well-known pseudo-stationary form:

$$\nabla \bullet \boldsymbol{\sigma} = 0 \tag{6}$$

By considering a disk-shaped sample pressed in a cylindrical die, Eqs. (3) and (6) can be written down in cylindrical coordinates:

$$\frac{\partial \rho}{\partial t} + \frac{1}{r}\frac{\partial}{\partial r}(\rho r v_r) + \frac{1}{r}\frac{\partial}{\partial \vartheta}(\rho v_\vartheta) + \frac{\partial}{\partial z}(\rho v_z) = 0 \tag{7}$$

$$\frac{1}{r}\frac{\partial}{\partial r}(r\sigma_{rr}) + \frac{1}{r}\frac{\partial \sigma_{r\vartheta}}{\partial \vartheta} + \frac{\partial \sigma_{rz}}{\partial z} - \frac{\sigma_{\vartheta\vartheta}}{r} = 0 \tag{8a}$$

$$\frac{1}{r^2}\frac{\partial}{\partial r}\left(r^2\sigma_{r\vartheta}\right) + \frac{1}{r}\frac{\partial \sigma_{\vartheta\vartheta}}{\partial \vartheta} + \frac{\partial \sigma_{\vartheta z}}{\partial z} = 0 \tag{8b}$$

$$\frac{1}{r}\frac{\partial}{\partial r}(r\sigma_{rz}) + \frac{1}{r}\frac{\partial \sigma_{\vartheta z}}{\partial \vartheta} + \frac{\partial \sigma_{zz}}{\partial z} = 0 \tag{8c}$$

By taking advantage of the usual axial symmetry assumption and neglecting friction between the consolidating powders and the (rigid) die internal wall (leading to negligible shear stresses), Eqs. (7) and (8) simplify as follows:

$$\frac{\partial \rho}{\partial t} + \frac{\partial}{\partial z}(\rho v_z) = 0 \tag{9}$$

$$\frac{1}{r}\frac{\partial}{\partial r}(r\sigma_{rr}) - \frac{\sigma_{\vartheta\vartheta}}{r} = 0 \tag{10a}$$

$$\frac{\partial \sigma_{zz}}{\partial z} = 0 \tag{10b}$$

By assuming a spatially uniform distribution of the density and neglecting radial gradients, the following system governing equations holds:

$$\frac{\partial \rho}{\partial t} + \rho\frac{\partial v_z}{\partial z} = 0 \tag{11}$$

$$\sigma_{rr} = \sigma_{\vartheta\vartheta} \tag{12a}$$

$$\frac{\partial \sigma_{zz}}{\partial z} = 0 \tag{12b}$$

The connection between the strain tensor and the velocity field is given by the strain rate tensor defined as follows:

$$\dot{\boldsymbol{\varepsilon}} = \frac{d\boldsymbol{\varepsilon}}{dt} = \frac{1}{2}\left(\nabla \vec{v} + \nabla \vec{v}^T\right) \tag{13}$$

Under the simplifying conditions mentioned above, Eq. (13) reduces to

$$\dot{\varepsilon}_{zz} = \frac{d\varepsilon_{zz}}{dt} = \frac{\partial v_z}{\partial z} \tag{14}$$

and, after substituting Eq. (14) into Eq. (11) and expressing Eq. (1) in terms of strain rate, the following governing equation of the sample density is obtained:

$$\frac{d\rho}{dt} = -\rho\left(\frac{d\varepsilon_{zz,1}^P}{dt} + \frac{d\varepsilon_{zz,2}^{VP}}{dt}\right) \tag{15}$$

Eq. (15) restates that the sample density evolution is given by the sum of the plastic deformation of Element 1 and the viscoplastic

consolidation of Element 2. Note that the partial derivative has been replaced by the ordinary one since density is assumed spatially uniform (only time dependent). In what follows the constitutive relations for bodies (1) and (2) are described.

2.1. Plastic deformation of Body (1)

Let us assume that Body (1) behaves as a perfectly plastic porous body (elasticity is neglected). Under the same assumptions illustrated in the previous paragraph (pressing in a rigid die), the variation of the plastic strain tensor components can be expressed by the flow rule [22,23]:

$$d\varepsilon_{ij}^{P} = d\Lambda \frac{\partial \Psi^{P}}{\partial \sigma_{ij}} \tag{16}$$

where Ψ^{P} is the plastic potential, σ_{ij} are the Cauchy stress tensor components, and Λ is the plastic multiplier. By assuming an associated flow rule, the plastic potential equals the yield function F [24–26] such that

$$d\varepsilon_{ij}^{P} = d\Lambda \frac{\partial F}{\partial \sigma_{ij}} \tag{17}$$

The yield function is given by the following expression [24–26]:

$$F = \sigma_{eq}\left(\sigma_{ij}, \rho\right) - \sigma_{Y}(\rho, T) \tag{18}$$

where T is the temperature. The equivalent stress σ_{eq} is defined as follows [27–29]:

$$\sigma_{eq} = \left[A(\rho)J_2 + B(\rho)I_1^2\right]^{1/2} \tag{19}$$

where $A(\rho)$ and $B(\rho)$ are empirical constants depending on relative density ρ. J_2 is the second invariant of the deviatoric Cauchy stress tensor:

$$J_2 = \frac{1}{2}\sigma_{ij}^{'}\sigma_{ij}^{'} \tag{20}$$

while I_1 is the first invariant of the Cauchy stress tensor:

$$I_1 = tr(\boldsymbol{\sigma}) \tag{21}$$

where $tr(\boldsymbol{\sigma})$ indicates the trace of the tensor, and $\sigma_{ij}^{'}$ are the deviatoric Cauchy tensor components defined as:

$$\sigma_{ij}^{'} = \sigma_{ij} - \frac{I_1}{3}\delta_{ij} \tag{22}$$

where δ_{ij} represents the Kronecker delta.

As defined by Eq. (18), F is a function of the variables σ_{ij}, ρ, and T. The consistency condition can be then written down as follows:

$$dF = \frac{\partial F}{\partial \sigma_{ij}}d\sigma_{ij} + \frac{\partial F}{\partial \rho}d\rho + \frac{\partial F}{\partial T}dT = 0 \tag{23}$$

The mass conservation principle (continuity equation) leads to:

$$d\rho = -\rho\ \mathrm{tr}\left(d\boldsymbol{\varepsilon}^{P}\right) \tag{24}$$

which using Eq. (17) can be written as follows:

$$d\rho = -\rho d\Lambda tr\left(\frac{\partial F}{\partial \sigma_{ij}}\right) \tag{25}$$

Inserting Eq. (25) into Eq. (23)

$$\frac{\partial F}{\partial \sigma_{ij}}d\sigma_{ij} - \frac{\partial F}{\partial \rho}\rho d\Lambda tr\left(\frac{\partial F}{\partial \sigma_{ij}}\right) + \frac{\partial F}{\partial T}dT = 0 \tag{26}$$

and solving for $d\Lambda$ yields:

$$d\Lambda = \frac{\frac{\partial F}{\partial \sigma_{ij}}d\sigma_{ij} + \frac{\partial F}{\partial T}dT}{\rho\frac{\partial F}{\partial \rho}tr\left(\frac{\partial F}{\partial \sigma_{ij}}\right)} \tag{27}$$

Substituting Eq. (27) into Eq. (17), it can be obtained that

$$d\varepsilon_{ij}^{P} = \frac{\left(\frac{\partial F}{\partial \sigma_{ij}}\right)^{2}d\sigma_{ij} + \left(\frac{\partial F}{\partial \sigma_{ij}}\right)\frac{\partial F}{\partial T}dT}{\rho\frac{\partial F}{\partial \rho}tr\left(\frac{\partial F}{\partial \sigma_{ij}}\right)} \tag{28}$$

It is also that (cf. Eq.(18))

$$\frac{\partial F}{\partial \sigma_{ij}} = \frac{\partial}{\partial \sigma_{ij}}\left(\sigma_{eq} - \sigma_{Y}\right) = \frac{\partial \sigma_{eq}}{\partial \sigma_{ij}} \tag{29}$$

$$\frac{\partial F}{\partial \rho} = \frac{\partial}{\partial \rho}\left(\sigma_{eq} - \sigma_{Y}\right) = \frac{\partial \sigma_{eq}}{\partial \rho} - \frac{\partial \sigma_{Y}}{\partial \rho} \tag{30}$$

$$\frac{\partial F}{\partial T} = \frac{\partial}{\partial T}\left(\sigma_{eq} - \sigma_{Y}\right) = -\frac{\partial \sigma_{Y}}{\partial T} \tag{31}$$

Then Eq. (28) becomes:

$$d\varepsilon_{ij}^{P} = \frac{\left(\frac{\partial \sigma_{eq}}{\partial \sigma_{ij}}\right)^{2}d\sigma_{ij} - \left(\frac{\partial \sigma_{eq}}{\partial \sigma_{ij}}\right)\frac{\partial \sigma_{Y}}{\partial T}dT}{\rho\left(\frac{\partial \sigma_{eq}}{\partial \rho} - \frac{\partial \sigma_{Y}}{\partial \rho}\right)tr\left(\frac{\partial \sigma_{eq}}{\partial \sigma_{ij}}\right)} \tag{32}$$

Recalling Eq. (19), it can be derived that

$$\frac{\partial \sigma_{eq}}{\partial \sigma_{ij}} = \frac{1}{2\sigma_{eq}}\left[A\sigma_{ij} - \left(\frac{1}{3}A - 2B\right)I_1\delta_{ij}\right] \tag{33}$$

For the sake of shorter notation let us define

$$\Sigma_{ij} = A\sigma_{ij} - \left(\frac{1}{3}A - 2B\right)I_1\delta_{ij} \tag{34}$$

such that Eq. (32) can be re-written as:

$$d\varepsilon_{ij}^{P} = \frac{\frac{1}{2\sigma_{eq}}\left(\Sigma_{ij}\right)^{2}d\sigma_{ij} - \Sigma_{ij}\frac{\partial \sigma_{Y}}{\partial T}dT}{\rho\left(\frac{\partial \sigma_{eq}}{\partial \rho} - \frac{\partial \sigma_{Y}}{\partial \rho}\right)tr(\boldsymbol{\Sigma})} \tag{35}$$

Conveying the trace of tensor $\boldsymbol{\Sigma}$ in cylindrical coordinates gives

$$tr(\boldsymbol{\Sigma}) = 6BI_1 \tag{36}$$

and substituting Eq. (36) into Eq. (35) yields:

$$d\varepsilon_{ij}^{P} = \frac{\frac{1}{2\sigma_{eq}}\left(\Sigma_{ij}\right)^{2}d\sigma_{ij} - \Sigma_{ij}\frac{\partial \sigma_{Y}}{\partial T}dT}{6\rho\left(\frac{\partial \sigma_{eq}}{\partial \rho} - \frac{\partial \sigma_{Y}}{\partial \rho}\right)\ BI_1} \tag{37}$$

According to the assumption of densification taking place in a rigid cylindrical die, it follows that $\varepsilon_{rr}^{P} = \varepsilon_{\vartheta\vartheta}^{P} = 0$. Then, applying Eq. (37) to the unique non-null component of the strain tensor and expressing Eq. (37) in terms of temporal variation, the first term on the r.h.s. of Eq. (15) is obtained:

$$\frac{d\varepsilon_{zz,1}^{P}}{dt} = \dot{\varepsilon}_{zz,1}^{P} = \frac{\frac{1}{2\sigma_{eq}}\left(\Sigma_{zz}\right)^{2}\frac{d\sigma_{zz}}{dt} - \Sigma_{zz}\frac{\partial \sigma_{Y}}{\partial T}\frac{dT}{dt}}{6\rho\left(\frac{\partial \sigma_{eq}}{\partial \rho} - \frac{\partial \sigma_{Y}}{\partial \rho}\right)\ BI_1} \tag{38}$$

where it can be clearly seen that the dynamics of the plastic deformation of Element 1 is determined by the temporal variations of the applied stress σ_{zz} and temperature T.

To solve Eq. (38) the value of I_1 is needed. In the case of cylindrical coordinates, the first invariant is given by:

$$I_1 = \sigma_{rr} + \sigma_{\vartheta\vartheta} + \sigma_{zz} \tag{39}$$

where σ_{rr} and $\sigma_{\vartheta\vartheta}$ are the radial and the hoop stresses, respectively, generated inside the sample by the application of the external load σ_{zz}. By introducing the contact pressure p exerted by the sample to the die internal wall, under the adopted simplifying assumptions (cf. Eq. (12a)), it follows that

$$\sigma_{rr} = \sigma_{\vartheta\vartheta} = -p \tag{40}$$

Accordingly,

$$I_1 = \sigma_{zz} - 2p \tag{41}$$

To find the stress p, Eq. (38) is applied to the null components of the plastic strain tensor:

$$0 = \frac{\frac{1}{2\sigma_{eq}}(\Sigma_{\alpha\alpha})^2 \frac{d\sigma_{\alpha\alpha}}{dt} - \Sigma_{\alpha\alpha}\frac{\partial\sigma_Y}{\partial T}\frac{dT}{dt}}{6\rho\left(\frac{\partial\sigma_{eq}}{\partial\rho} - \frac{\partial\sigma_Y}{\partial\rho}\right) 6BI_1} \tag{42}$$

where subscript α can be either r or ϑ, respectively. Eq. (42) is verified if

$$\frac{1}{2\sigma_{eq}}(\Sigma_{\alpha\alpha})^2 \frac{d\sigma_{\alpha\alpha}}{dt} - \Sigma_{\alpha\alpha}\frac{\partial\sigma_Y}{\partial T}\frac{dT}{dt} = 0 \tag{43}$$

Eq. (43) should be verified whatever the operating conditions (i.e., $\frac{dT}{dt}, \frac{d\sigma_{\alpha\alpha}}{dt}$) and yield strength temperature dependence (i.e., $\frac{\partial\sigma_Y}{\partial T}$) are. Taking the special case of isothermal compression and constant stress components leads to the condition

$$\Sigma_{\alpha\alpha} = 0 \tag{44}$$

Recalling Eqs. (34) and (41) yields

$$p = -\frac{\left(\frac{1}{3}A - 2B\right)}{\left(\frac{1}{3}A + 4B\right)}\sigma_{zz} \tag{45}$$

2.2. Viscoplastic consolidation of Body (2)

To establish a thermodynamically consistent formulation of the stress-strain rate constitutive law, a dissipation potential-based approach inspired by the procedure introduced by Olevsky is adopted [11]. Within this framework, the constitutive relationship governing the dashpot element is derived ensuring convexity and compliance with the second law of thermodynamics. In parallel, it is shown that the viscoplastic potential that defines the yield function associated with the slider (cf. 2.1) is dual to the selected dissipation potential, meaning that they describe complementary aspects of the material response. This duality highlights the internal consistency of the model and provides further justification for the combined use of slider and dashpot elements to capture the distinct mechanisms active during pressure-assisted sintering.

2.2.1. Derivation of stress–strain rate relation

To describe the viscoplastic behavior of the Bingham fluid modeled by a rheological element consisting of a slider and a dashpot in parallel (as illustrated in Fig. 1), the following dissipation potential is defined:

$$\Phi(\dot{\varepsilon}_{ij}) = 2\eta\dot{\gamma}^2 + \frac{1}{2}\kappa tr(\dot{\boldsymbol{\varepsilon}})^2 + (1-\theta)\frac{\sigma_Y^2}{6\eta^*} \tag{46}$$

where $\dot{\gamma}$ is the second invariant of the strain rate tensor deviator $\dot{\boldsymbol{\varepsilon}}'$ and $\theta = 1 - \rho$ represents the sample porosity.

The first term of Eq. (46) represents the viscous deformation of Body (2) (cf. Fig. 1) while its compressibility is expressed by the second term. The last one makes the porous material behaving as a Bingham fluid whose deformation occurs if the applied equivalent stress σ_{eq} exceeds the yield strength of the (pore-free) material, $\sigma_{Y,2}$. The shear (η) and bulk (κ) viscosities of the compacting (porous) sample can be expressed as follows [11]:

$$\eta = \varphi\eta^* \tag{47}$$

$$\kappa = \psi\kappa^* = 2\psi\eta^* \tag{48}$$

where φ and ψ are functions of the sample porosity (see Table 1), and η^* and κ^* are the shear and bulk viscosity of the dense (pore-free) matrix material, respectively.

The stress-strain rate relationship can be obtained as:

$$\sigma_{ij} = \frac{\partial\Phi}{\partial\dot{\varepsilon}_{ij}} \tag{49}$$

that gives

$$\sigma_{ij} = 2\eta\dot{\varepsilon}'_{ij} + \kappa tr(\dot{\boldsymbol{\varepsilon}})\delta_{ij} \tag{50}$$

Recalling that

$$\sigma_{ij} = \sigma'_{ij} + \frac{1}{3}tr(\boldsymbol{\sigma})\delta_{ij} \tag{51}$$

and comparing Eqs. (50) and (51) results that

$$\sigma'_{ij} = 2\eta\dot{\varepsilon}'_{ij} \tag{52}$$

and

$$\frac{1}{3}tr(\boldsymbol{\sigma}) = \kappa tr(\dot{\boldsymbol{\varepsilon}}) \tag{53}$$

Expressing Eq. (50) in terms of the strain rate tensor instead of its deviator yields

Table 1
Summary of constitutive dependencies for temperature-, porosity-, and strain rate-sensitive model parameters used in this work.

Quantity	Functionality	Reference
$\sigma_{eq}(\theta)$	$\left[A(\theta)J_2 + B(\theta)I_1^2\right]^{1/2}$	[29]
$A(\theta)$	$\frac{3}{(1-\theta)\varphi}$	This work
$B(\theta)$	$\frac{1}{6(1-\theta)\psi}$	This work
$\varphi(\theta)$	$(1-\theta)^2$	[11]
$\psi(\theta)$	$\frac{(1-\theta)^3}{\theta}$	This work
$\sigma_Y(T)$	$\sigma_Y^\infty + (\sigma_Y^0 - \sigma_Y^\infty)\left[1 + \exp\left(\frac{T-A_T}{B_T}\right)\right]^{-1}$	[34]
$\frac{\partial\sigma_{eq}}{\partial\theta}$	$\frac{1}{2\sigma_{eq}}\left(\frac{\partial A}{\partial\theta}J_2 + \frac{\partial B}{\partial\theta}I_1^2 + \frac{\partial J_2}{\partial\theta}A + 2BI_1\frac{\partial I_1}{\partial\theta}\right)$	This work
$\frac{\partial A}{\partial\theta}$	$\frac{9}{(1-\theta)^4}$	This work
$\frac{\partial B}{\partial\theta}$	$\frac{1}{6}\frac{3\theta+1}{(1-\theta)^5}$	This work
$\frac{\partial J_2}{\partial\theta}$	$\frac{2}{3}(p - \sigma_{app})\frac{\partial p}{\partial\theta}$	This work
$\frac{\partial I_1}{\partial\theta}$	$-2\frac{\partial p}{\partial\theta}$	This work
$\frac{\partial p}{\partial\theta}$	$\frac{2p}{\left(\frac{1}{9}A^2 + \frac{2}{3}AB - 8B^2\right)}\left(B\frac{dA}{d\theta} - A\frac{dB}{d\theta}\right)$	This work
$\frac{\partial\sigma_Y}{\partial\theta}$	0	This work
$\frac{\partial\sigma_Y}{\partial T}$	$-\frac{(\sigma_Y^0 - \sigma_Y^\infty)\exp\left(\frac{T-A_T}{B_T}\right)}{B_T\left[1 + \exp\left(\frac{T-A_T}{B_T}\right)\right]^2}$	This work
$\frac{d\sigma_{zz}}{dt}$	0	This work
$\frac{dT}{dt}$	see experimental details reported in the text	This work

$$\sigma_{ij} = 2\eta\dot{\varepsilon}_{ij} + \left(\kappa - \frac{2}{3}\eta\right) tr(\dot{\boldsymbol{\varepsilon}})\delta_{ij} \tag{54}$$

2.2.2. Duality between dissipation Φ and viscoplastic Ψ potentials

The thermodynamic consistency of the model is further supported by showing that the dissipation potential introduced in the previous section to define the response of Element 2 to the applied load is dual to the viscoplastic potential governing the sliders, thereby linking in a consistent way the stress–strain rate relationship (54) with the yield criterion adopted in 2.1.

Assigned the dissipation potential $\Phi(\dot{\varepsilon}_{ij})$ defined by Eq. (46), the viscoplastic potential $\Psi(\sigma_{ij})$ is given by the following Legendre-Fenchel transform [30,31]:

$$\Psi(\sigma_{ij}) = \sup_{\dot{\varepsilon}_{ij}} \{\dot{\varepsilon}_{ij}\sigma_{ij} - \Phi(\dot{\varepsilon}_{ij})\} \tag{55}$$

and substituting Eq. (46) into Eq. (55) leads to

$$\Psi(\sigma_{ij}) = \sup_{\dot{\varepsilon}_{ij}} \left\{\dot{\varepsilon}_{ij}\sigma_{ij} - \eta\dot{\varepsilon}'_{ij}\dot{\varepsilon}'_{ij} - \frac{1}{2}\kappa tr(\dot{\boldsymbol{\varepsilon}})^2 - (1-\theta)\frac{\sigma_Y^2}{6\eta^*}\right\} \tag{56}$$

Decomposing the stress and strain rate tensors and recalling that tensors $\boldsymbol{\sigma}'$ and $\boldsymbol{\varepsilon}'$ are traceless, Eq. (56) is expressed as follows:

$$\Psi(\sigma_{ij}) = \sup_{\dot{\varepsilon}'_{ij}} \left\{\sigma'_{ij}\dot{\varepsilon}'_{ij} + \frac{1}{3}tr(\dot{\boldsymbol{\varepsilon}})tr(\boldsymbol{\sigma}) - \eta\dot{\varepsilon}'_{ij}\dot{\varepsilon}'_{ij} - \frac{1}{2}\kappa tr(\dot{\boldsymbol{\varepsilon}})^2 - (1-\theta)\frac{\sigma_Y^2}{6\eta^*}\right\} \tag{57}$$

Eq. (57) can be separated into two independent maximizations:

$$\Psi(\sigma_{ij}) = \sup_{\dot{\varepsilon}'_{ij}} \left\{\sigma'_{ij}\dot{\varepsilon}'_{ij} - \eta\dot{\varepsilon}'_{ij}\dot{\varepsilon}'_{ij}\right\} + \sup_{e} \left\{\frac{1}{3}tr(\boldsymbol{\sigma})tr(\dot{\boldsymbol{\varepsilon}}) - \frac{1}{2}\kappa tr(\dot{\boldsymbol{\varepsilon}})^2 - (1-\theta)\frac{\sigma_Y^2}{6\eta^*}\right\} \tag{58}$$

Maximation of the first term

$$\frac{\partial}{\partial\dot{\varepsilon}'_{ij}}\left(\sigma'_{ij}\dot{\varepsilon}'_{ij} - \eta\dot{\varepsilon}'_{ij}\dot{\varepsilon}'_{ij}\right) = 0 \tag{59}$$

gives

$$\dot{\varepsilon}'_{ij} = \frac{\sigma'_{ij}}{2\eta} \tag{60}$$

and substituting Eq. (60) into the first term of Eq. (58) yields

$$\sup_{\dot{\varepsilon}'_{ij}} \left\{\sigma'_{ij}\dot{\varepsilon}'_{ij} - \eta\dot{\varepsilon}'_{ij}\dot{\varepsilon}'_{ij}\right\} = \frac{\sigma'_{ij}\sigma'_{ij}}{4\eta} \tag{61}$$

Calculating the supremum expressed by the second term of Eq. (58)

$$\frac{\partial}{\partial e}\left(\frac{1}{3}tr(\boldsymbol{\sigma})tr(\dot{\boldsymbol{\varepsilon}}) - \frac{1}{2}\kappa tr(\dot{\boldsymbol{\varepsilon}})^2 - (1-\theta)\frac{\sigma_Y^2}{6\eta^*}\right) = 0 \tag{62}$$

yields

$$tr(\dot{\boldsymbol{\varepsilon}}) = \frac{tr(\boldsymbol{\sigma})}{3\kappa} \tag{63}$$

Substituting Eq. (63) into the second term of Eq. (58) results in

$$\sup_{e} \left\{\frac{1}{3}tr(\boldsymbol{\sigma})tr(\dot{\boldsymbol{\varepsilon}}) - \frac{1}{2}\kappa tr(\dot{\boldsymbol{\varepsilon}})^2 - (1-\theta)\frac{\sigma_Y^2}{6\eta^*}\right\} = \frac{1}{18\kappa}(tr(\boldsymbol{\sigma}))^2 - (1-\theta)\frac{\sigma_Y^2}{6\eta^*} \tag{64}$$

Summing up Eqs. (61) and (64), the expression of the viscoplastic potential can be obtained:

$$\Psi(\sigma_{ij}) = \frac{1}{2\eta}J_2 + \frac{1}{18\kappa}I_1^2 - (1-\theta)\frac{\sigma_Y^2}{6\eta^*} \tag{65}$$

Inserting Eqs. (47) and (48), rearranging and recalling Eq. (19) leads to the following final form of Ψ:

$$\Psi(\sigma_{ij}) = \frac{(1-\theta)}{6\eta^*}\left(\sigma_{eq}^2 - \sigma_Y^2\right) \tag{66}$$

By equating to zero Eq. (66), the yield function F adopted in 2.1 is attained. Notably, if $\theta \to 0$ the Von Mises definition of equivalent stress ($\sigma_{eq} = \sqrt{3J_2}$) and the corresponding yield criterion can be derived.

2.2.3. Application to uniaxial pressing in a rigid cylindrical die and material viscosity functionality

The stress–strain rate relationship derived in 2.2.1 is now applied to the case of uniaxial pressure-assisted sintering in a rigid cylindrical die, corresponding to the experimental setup used in this study. Applying Eq. (54) under the already mentioned simplifying assumptions, the following expression for the stress and strain rate relationship is obtained:

$$\frac{d\varepsilon_{zz}^{VP}}{dt} = \dot{\varepsilon}_{zz} = \frac{\sigma_{zz}}{\mu} \tag{67}$$

that computes the second contribution appearing on the r.h.s. of Eq. (15). The apparent viscosity μ of the densifying sample introduced in Eq. (67) is defined as

$$\mu = \kappa + \frac{4}{3}\eta \tag{68}$$

This property quantifies the total viscous resistance of the porous compact to densification. It integrates the effects of both shape-preserving and volume-reducing deformations, thus providing a meaningful macroscopic indicator of sinterability under combined thermo-mechanical loading.

As for the evolving thermomechanical conditions during densification, the material viscosity μ must be expressed as a function of temperature, porosity, and equivalent strain rate. In particular, the latter dependence is captured using the Bird–Carreau model, which allows a continuous transition between Newtonian and shear-thinning behavior without imposing a priori a linear or non-linear behavior [32,33]. By also considering Eqs. (47) and (48), the apparent viscosity of the consolidating sample can be comprehensively expressed as follows:

$$\mu(T,\theta,\dot{\varepsilon}_{zz}) = \eta^0(T)\frac{4}{3}\left(\varphi + \frac{3}{2}\psi\right)[1 + \lambda(T)W]^{m-1} \tag{69}$$

where m is the strain-rate sensitivity coefficient and W is the equivalent strain rate defined by

$$W = f(\theta)|\dot{\varepsilon}_{zz}| \tag{70}$$

with

$$f(\theta) = \sqrt{\frac{\frac{4}{9}\varphi + \frac{2}{3}\psi}{(1-\theta)}} \tag{71}$$

The first factor in Eq. (69), η^0, represents the zero-shear rate viscosity of dense (pore-free) material whose temperature dependence is taken as

$$\eta^0 = a^0 \exp\left(\frac{Q_\eta}{RT}\right) \tag{72}$$

Finally, the parameter λ, which appears in Eq. (69), characterizes the strain-rate time scale at which the material transitions from Newtonian (linear) to shear-thinning (nonlinear) behavior. Physically, it can be interpreted as a material-specific relaxation time: the characteristic timescale over which the microstructure can respond viscously to applied stress. When the inverse of the equivalent strain rate (W^{-1}) is large compared to λ, the material deforms linearly; as the strain rate increases and becomes comparable to or exceeds λ^{-1}, nonlinear effects become significant. During pressure-assisted sintering, this transition is influenced by temperature, porosity evolution, and particle interactions,

making λ a key parameter that bridges microscopic flow mechanisms and macroscopic deformation behavior. For the sake of simplicity, in this work only the temperature dependence is accounted for through the following relation [33]:

$$\lambda(T) = \lambda^0 T^{\left(\frac{m}{m-1}\right)} \exp\left(\frac{Q_\eta}{RT}\right) \tag{73}$$

2.3. Constitutive parameter dependencies

The rheological behavior of the TMB powder during densification is governed not only by its mechanical structure but also by the evolution of key material properties, such as shear viscosity, bulk viscosity, and yield strength, as functions of temperature, porosity, and strain rate. The constitutive relationships adopted here to describe these dependencies are essential for accurately describing the nonlinear viscoplastic response of the system under varying SPS conditions. For clarity, all functional forms, auxiliary relations, and dependencies are summarized in Table 1. It is worth mentioning that, in this work, the yield strength σ_Y is taken as a function of temperature only, while lumping the porosity effect on the equivalent stress (cf. Eq. (19)) [27,28].

Fig. 2 graphically illustrates the selected temperature-dependent evolution of the yield strength σ_Y associated with the slider elements in the proposed rheological model. The curve shows the smooth transition from the low-temperature asymptotic value σ_Y^0 to the high-temperature asymptotic value σ_Y^∞, thus elucidating the effect of temperature on the particle rearrangement (Body (1)) or material matrix thermal softening (Body (2)). This transition is controlled by two parameters: A_T, which defines the midpoint temperature of the shift, and B_T, which characterizes the shift steepness. At low temperatures ($T \ll A_T$), σ_Y approaches σ_Y^0 representing the high resistance to plastic rearrangement (Body (1)) or to material deformation when atomic mobility is limited (Body (2)). At high temperatures ($T \gg A_T$), the yield strength decreases toward σ_Y^∞, reflecting the enhanced packability of the particle network (Body (1)) or the material deformability (Body (2)) as the temperature increases. The sigmoidal shape of the curve allows a smooth albeit remarkable transition, consistent with the onset of the significant thermal activation typically observed during sintering of

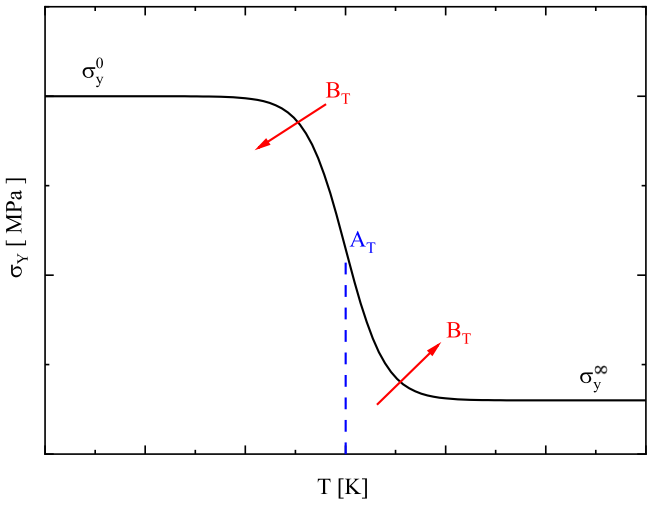

Fig. 2. Temperature-dependent yield strength σ_Y used in the proposed model. The curve captures the transition from the low-temperature yield strength σ_Y^0 to the high-temperature asymptotic value σ_Y^∞, following a sigmoidal decay. The parameters A_T and B_T define the temperature at which the transition occurs and sharpness of this transition, respectively. This behavior reflects the thermally activated particle interaction (Body (1)) or the continuous matrix softening (Body (2)) and plays a central role in regulating the onset of the different mechanisms within the rheological model shown in Fig. 1.

TMBs. In particular, as far as the slider of Element 1 is concerned, this function ensures that such model component is only active within a limited temperature range during early heating while it automatically deactivates as temperature rises and the material behavior becomes dominated by viscous deformation.

2.4. Model parameter calculation and fitting procedure

The proposed mathematical model involves eight parameters to be determined. To reduce the number of adjustable ones and the risk of overfitting, a three-steps strategy was applied, leveraging physical insights (cf. Fig. 2), as well as taking advantage of the available experimental data and adopted operating conditions. First step involves the calculation of $\sigma_{Y,1}^0$ and A_T by analyzing specific points of the experimental porosity time-profile. Only the first part of the latter is then used to fit the parameters $\sigma_{Y,1}^\infty$ and B_T, thus completing the determination of the slider parameter set. Finally, the remaining four parameters (i.e., those ones related to the dashpot) are fitted by using the entire porosity time-profile. Each step is described in detail in what follows.

At the end of the powder pre-compaction step, the sample is still at room temperature, and its porosity θ^0 depends solely on the externally applied load. Under these low-temperature conditions, particle rearrangement is the only active consolidation mechanism. As such, the material behaves as a perfectly plastic solid, and the equivalent stress within the compact must equal its yield strength: $\sigma_{eq}(\theta = \theta^0) = \sigma_{Y,1}(T = T^0)$, or stated differently and limited to the used experimental data, $\sigma_{eq}^0 \approx \sigma_{Y,1}^0$. Given that σ_{eq}^0 can be analytically calculated from the initial porosity, using the relations reported in 2.1 and Table 1, the value of $\sigma_{Y,1}^0$ is obtained. Table 2 reports the corresponding values used for each material in this initial calibration step. This procedure allows to indirectly estimate one of the yield parameters, thus reducing the number of parameters to be determined to seven.

Additional reduction on the latter comes from the analysis of the experimental porosity time evolution (shown in the next section). Since, under the adopted experimental conditions, during the first period of consolidation, particle rearrangement is directly linked to the evolution of $\sigma_{Y,1}$, the first inflection point in the porosity curve is assumed to correspond to the inflection point in the $\sigma_{Y,1} - T$ curve (cf. Fig. 2). Given the known heating profile and the experimentally determined time instant corresponding to the porosity profile inflection point, the parameter A_T can be estimated prior to the fitting process, thus further reducing the number of unknown parameters to six.

Moreover, since it is assumed that during the early stage of consolidation particle rearrangement is the only mechanism active for all the investigated materials (NbB_2, HfB_2, TiB_2), the corresponding data segment was used to fit the remaining two yield strength parameters, $\sigma_{Y,1}^\infty$ and B_T. The remaining model parameters, including viscosity-related ones, were estimated by fitting the full porosity-time profile over the entire sintering cycle. A summary of all calculated and fitted model parameters is provided in Table 3, where they are explicitly labeled as either *calculated* (calc.) or *adjusted* (adj.) for clarity.

Finally, preliminary simulations revealed that, under the experimental conditions investigated in this study, the equivalent stress remains above the possible yield strength $\sigma_{Y,2}$ of the porous continuous matrix (Body (2)) throughout the densification cycle. As a result, the slider of Element 2 in the rheological model (cf. Fig. 1) remains inactive, and densification due to viscous deformation is never hindered.

Table 2
Initial values of some model variables.

Variable	HfB_2	NbB_2	TiB_2
θ^0 [−]	0.42574	0.43722	0.42001
σ_{eq}^0 [MPa]	39.648	41.507	38.755

Table 3
Summary of model parameters.

Material		HfB_2		NbB_2		TiB_2	
Parameter	**Type**	**Without Slider**	**Complete**	**Without Slider**	**Complete**	**Without Slider**	**Complete**
A_T[K]	Calc.	-	1074.6	-	1020.0	-	1045.7
$\sigma^{\infty}_{Y,1}$[MPa]	Adj.	-	34.855	-	36.508	-	33.354
B_T[K]	Adj.	-	62.607	-	33.487	-	35.786
$\sigma^{0}_{Y,1}$[MPa]	Calc.	-	39.648	-	41.507	-	38.755
a^0 [Pa • s]	Adj.	$1.1812\ 10^5$	$1.1456\ 10^5$	$6.6416\ 10^6$	$3.5161\ 10^6$	$5.6744\ 10^4$	$4.1093\ 10^4$
$Q_\eta \left[\frac{kJ}{mol}\right]$	Adj.	272.87	287.44	188.75	224.50	442.75	669.83
$\lambda^0 \left[\frac{s}{K^{\left(\frac{m}{m-1}\right)}}\right]$	Adj.	0.09534	0.11897	14.295	12.425	0.26040	0.27156
m [−]	Adj.	0.11469	0.12284	0.18970	0.19759	0.10817	0.07976
R^2		0.99890	0.99993	0.99841	0.99985	0.99710	0.99946

Therefore, since the exact values of $\sigma_{Y,2}$ are not needed in the simulated scenarios, $\sigma_{Y,2}$ was set to zero in the numerical implementation to reduce the number of fitting parameters. Nevertheless, the general formulation of the model, which includes both the slider and the dashpot in parallel for Element 2, has been retained to make it applicable to other systems or operating conditions where the yield strength of the porous

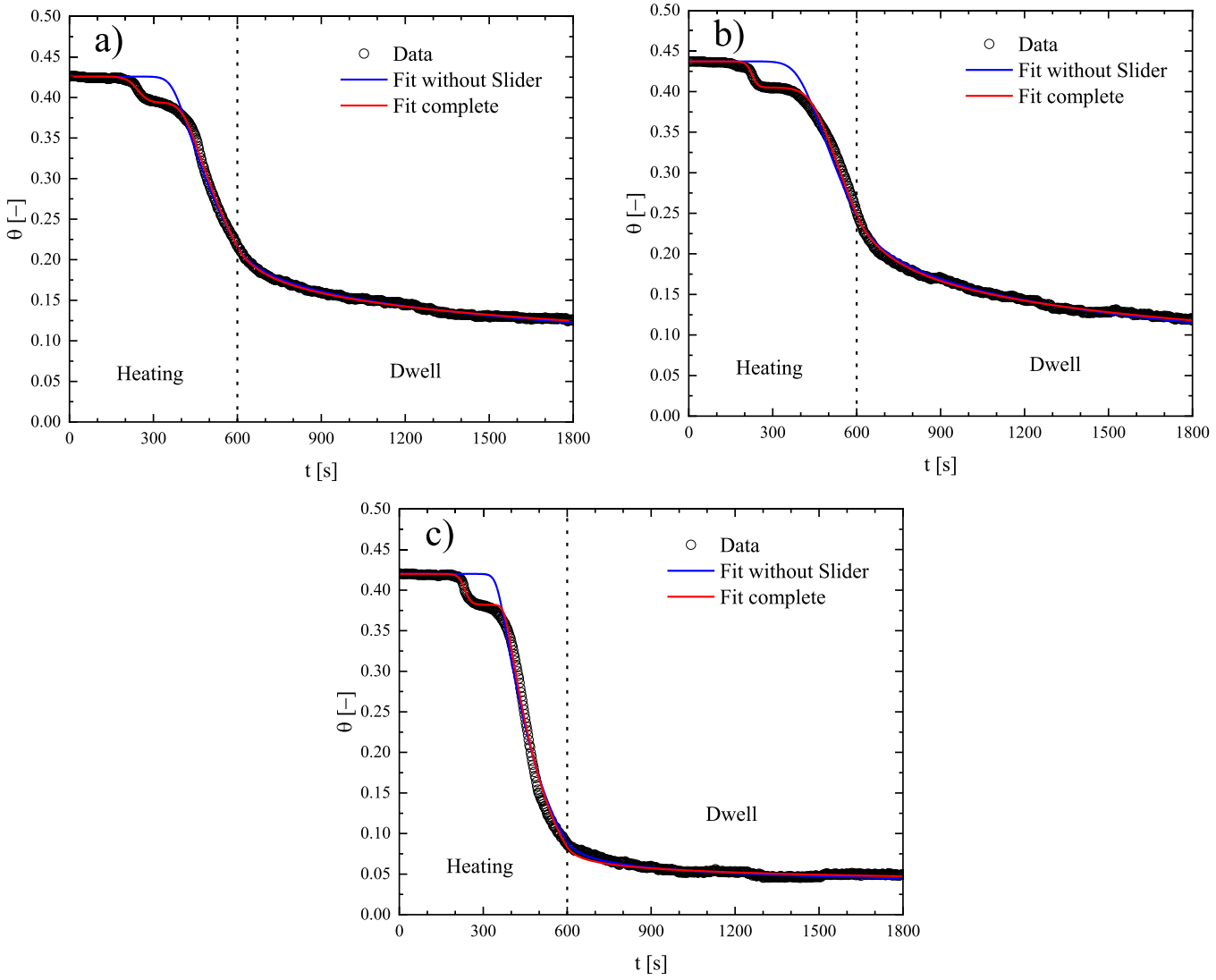

Fig. 3. Comparison between experimental and simulated porosity time profiles for a) HfB_2, b) NbB_2, and c) TiB_2 samples during SPS. Experimental data (black open circles) are fitted using two different modeling approaches: a complete model that includes both the slider and dashpot elements (red line), and a reduced model without the slider contribution (blue line). The temperature cycle consists of a heating stage up to 1950 °C in 10 min followed by a 20-minute isothermal dwell. The vertical dashed line indicates the transition between the non-isothermal heating and isothermal dwelling stages. The improved agreement achieved by the complete model highlights the importance of accounting for particle rearrangement to accurately simulate the densification behavior during the initial stages of sintering.

continuous matrix may play a more prominent role.

3. Results and discussion

3.1. Model fitting and mechanistic insights into densification behavior

Fig. 3a–c present the experimental and modeled porosity–time curves related to the spark plasma sintering of HfB_2, NbB_2, and TiB_2 powders, respectively, all processed under identical conditions: an applied pressure, σ_{app}, of 20 MPa, a heating time, t_H, from room to the desired temperature, of 10 min, a dwell temperature, T_D, of 1950 °C, and a dwell time, t_D, of 20 min. Additional experimental details are reported elsewhere [19]. Across all three materials, the porosity–time curve exhibits a characteristic multi-stage behavior. In the early part of the heating stage (up to ~300 s), a gradual decrease in porosity is observed despite the relatively low temperature. According to the proposed approach, this initial densification is attributed to particle rearrangement driven by the applied uniaxial pressure, a mechanism well modelled by the plastic slider component of the rheological model (cf. Fig. 1).

Following this initial rearrangement stage, a plateau appears in the curve of porosity, indicating a temporary halt in sample densification. This corresponds to an intermediate temperature range where neither particle rearrangement nor significant viscous flow is active. As the temperature continues to rise and exceeds a threshold at 300–400 s, viscous deformation starts to occur and becomes progressively dominant. This transition marks the onset of the dashpot-controlled regime. As the temperature increases further, viscous deformation results in a faster porosity decrease until the densification process smoothly enters into the dwell stage where the temperature is held constant.

Despite these shared characteristics, material-specific differences emerge in the shape and slope of the densification curves. HfB_2 (Fig. 3a) and NbB_2 (Fig. 3b) exhibit similar porosity evolution, with comparable timing and consolidation degree in both the rearrangement and viscous regimes. In contrast, TiB_2 (Fig. 3c) shows a steeper and more abrupt transition from the rearrangement stage to the viscous regime. The dwell phase begins at a lower porosity, and the overall densification is more pronounced than in the case of other materials.

Experimental data are compared in Fig. 3 with two model predictions: the complete rheological model (red line), which includes both particle rearrangement and viscous flow, and a reduced model (blue line) that considers only viscous deformation. The complete model accurately simulates both the early-stage rearrangement and the later viscous driven consolidation, closely matching the entire experimental curve. In contrast, the reduced model underestimates densification during the non-isothermal heating and fails to capture the initial drop in porosity. This demonstrates the necessity of including a distinct particle rearrangement mechanism to correctly describe the full sintering behavior of the investigated borides.

The comparison shown in Fig. 3 highlights the proposed model ability to accurately reproduce the experimental porosity evolution for all three TMBs under the selected SPS conditions. The improvement provided by the introduction of the slider element, particularly during the non-isothermal heating stage, underscores the need to account for a yield stress threshold governing particle rearrangement. To better understand the basis of this agreement, it is essential to examine the values of the material parameters used in the simulations.

Table 3 reports the full set of model parameters used to simulate the densification behavior of HfB_2, NbB_2, and TiB_2, for both the complete rheological model (with both slider and dashpot) and the simplified one (dashpot only). The high regression coefficients ($R^2 > 0.999$) for the complete model in all cases confirm the excellent agreement between simulations and experimental data. For all three diborides, the complete model includes a temperature-dependent yield strength σ_Y defined by four parameters: A_T, transition temperature (≈ 1020–1075 K); B_T transition width (≈ 33–63 K); σ_Y^0, low-temperature asymptotic yield stress (≈ 39–42 MPa); σ_Y^∞, high-temperature asymptotic yield stress (≈ 33–36 MPa).

As shown in Fig. 2, this sigmoidal behavior controls the activation and deactivation of the particle rearrangement mechanism. It is worth pointing out that the yield strength values reported in Table 3 should not be interpreted as an intrinsic mechanical property of the fully dense materials. Rather, they are indicators of the effective resistance to particle rearrangement within the porous compact during the early stages of sintering. As mentioned in 2, particle rearrangement is assumed to occur between rigid, undeformable particles, and the slider captures the onset of sliding or micro-slipping between them.

The temperature dependence of the yield strength does not intrinsically reflect bulk material softening but how a temperature increase facilitates abrasion, wearing, interparticle bonding disruption, oxide layer breaking and weakening, and, in general, all those phenomena which make rearrangement easier. This explains why the slider parameter values are similar across all three materials. In fact, they are governed primarily by powder characteristics, such as particle size distribution, surface condition, or packing heterogeneity, rather than intrinsic differences in the crystalline boride phases. Consequently, these parameters are best viewed as compact-level properties, instead of material constants. In this regard, it is worth mentioning that the boride powders were all produced according to the same technique and processed under identical conditions before undergoing SPS [19].

The viscous component of the model is characterized by the pre-exponential viscosity factor a^0, the activation energy for viscous flow Q_η, the coefficient λ^0 and the strain rate sensitivity m. Table 3 shows that activation energies vary significantly between materials: TiB_2 shows the highest value (≈ 670 kJ/mol), suggesting its greater thermal resistance to flow, while NbB_2 has the lowest one (≈ 225 kJ/mol). Analysis of the coefficient m reinforces earlier observations: TiB_2 has the lowest value (≈ 0.08), indicating pronounced nonlinearity and plastic-like flow under stress, while HfB_2 and NbB_2 exhibit higher m values (≈ 0.12–0.20), reflecting a more viscous-dominated response.

Importantly, the comparison between models (with vs. without slider) shows that omitting particle rearrangement leads to significantly different values for key parameters, particularly for a^0 and Q_η in the case of NbB_2 and TiB_2 (cf. Table 3). These discrepancies demonstrate how neglecting early-stage plasticity causes the model to compensate by inflating viscosity-related parameters, resulting in distorted material characterization. Moreover, the complete model yields slightly better fits in all cases, with R^2 values higher than its simplified version.

The simulated evolution of mechanical stresses during SPS of hafnium diboride, niobium diboride, and titanium diboride is shown in Fig. 4a–c, respectively. All simulations were performed under the same SPS conditions mentioned above. The plots display the time evolution of the equivalent stress σ_{eq} (red), the yield strength $\sigma_{Y,1}$ associated with particle rearrangement (blue), the applied axial stress σ_{app} (magenta), and the radial and hoop stresses p generated by the lateral constraint (green). For all three materials, simulations confirm the sequence of the consolidating mechanisms already identified in Fig. 3. It is apparent that an initial plastic regime, where $\sigma_{eq} = \sigma_{Y,1}$, indicating that particle rearrangement is active, is followed by a transition phase during which σ_{eq} drops below $\sigma_{Y,1}$. This marks the completion of plastic yielding, and the onset of a viscous-dominated regime.

For HfB_2 (Fig. 4a) and NbB_2 (Fig. 4b), the profiles are nearly identical. Both materials sustain plastic deformation until approximately 300 s, after which the equivalent stress decreases steadily as temperature increases, and viscous flow dominates. The yield strength of Element 1 (cf. Fig. 1) remains constant throughout, while the radial stress p gradually rises due to enhanced resistance to lateral flow as densification proceeds. These results reflect the similar rheological responses of these two borides, as well as their sintering kinetics observed in the corresponding porosity–time curves shown in Fig. 3a–b. While

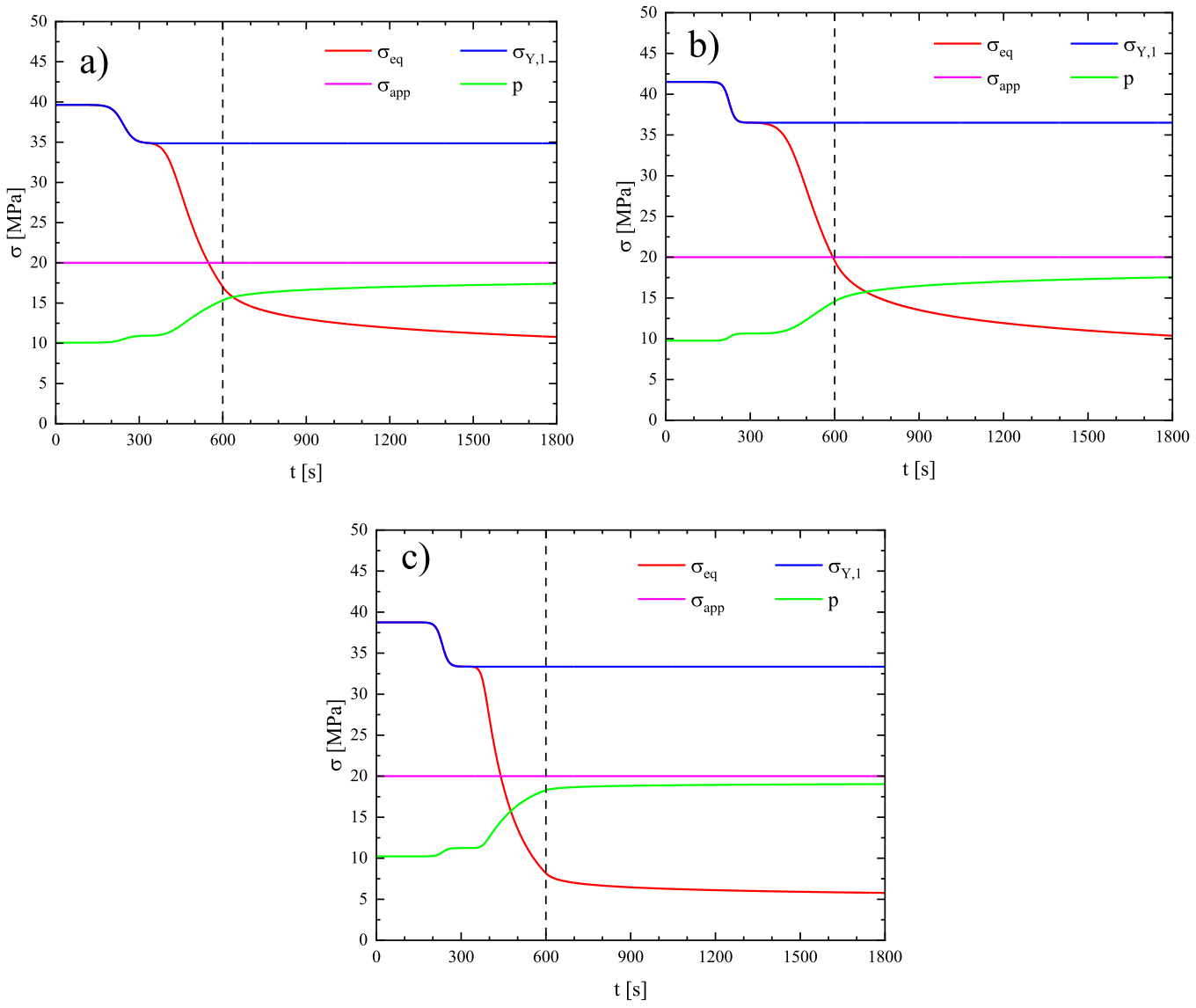

Fig. 4. Evolution of stress-related quantities during SPS at $\sigma_{app} = 20$ MPa, $t_H = 600$ s, $t_D = 1200$ s, and $T_D = 1950$ °C for: a) HfB_2, b) NbB_2, and c) TiB_2. Each panel shows the evolution of the equivalent stress (σ_{eq}, red), applied stress (σ_{app}, magenta), radial and hoop stresses (p, green), and yield stress ($\sigma_{Y,1}$, blue) as functions of time. The vertical dashed line marks the end of the heating stage ($t = 600$ s). In all cases, σ_{eq} drops below $\sigma_{Y,1}$ indicating that particle rearrangement ceases and only viscous deformation remains active. The evolution of p, which increases during densification, reflects the contribution to the consolidation behavior of each material due to the rigid die walls.

following the same general pattern, TiB_2 (Fig. 4c) displays clear distinctions. Although the transition from plastic to viscous behavior occurs at about the same time of the other borides, σ_{eq} decreases more sharply afterward. Additionally, the radial stress p increases more rapidly and reaches a higher final value, approaching the level of the applied uniaxial pressure closer than the other two borides. This behavior is consistent with the greater sensitivity to strain rate of the viscous deformation exhibited by TiB_2, as attested by its lower Bird–Carreau exponent m, confirming a more plastic-like behavior under elevated temperatures of this boride (cf. Table 3).

Overall, simulation results shown in Figs. 3 and 4 emphasize the importance of properly describing the interplay between stress state and deformation mechanism during SPS. The agreement between predicted stress evolution and densification trends validates the physical structure of the rheological model and suggests that early-stage plasticity followed by viscous flow governs the densification of transition metal diborides.

The stress profiles presented in Fig. 4 reveal when and how the plastic rearrangement mechanism becomes active or ceases during sintering, depending on the material and process conditions. To gain deeper insight into how this stress evolution translates into actual deformation behavior, Fig. 5 analyzes the associated strain rate profiles and the interplay between particle rearrangement and viscous flow across different pressures, materials, and activation energies. Fig. 5a shows the time evolution of the densification strain rate $\dot{\varepsilon}$ for HfB_2 (red), NbB_2 (green), and TiB_2 (blue) during SPS under identical processing conditions (20 MPa, 10-minute heating, 1950 °C dwell). The profiles are derived from the complete rheological model and reflect the interplay between particle rearrangement and viscous deformation across the sintering cycle. All three materials exhibit a non-monotonic strain rate evolution with two distinct peaks. The first peak, occurring early during heating (before ~300 s), corresponds to the particle rearrangement, driven by the applied pressure. A second, sharper peak in the 300–600 s time interval marks the transition into viscous-dominated deformation as the temperature approaches the dwell point. Among the three, TiB_2 shows the most pronounced and deepest minimum in strain rate, indicating a more abrupt and intense densification during the non-

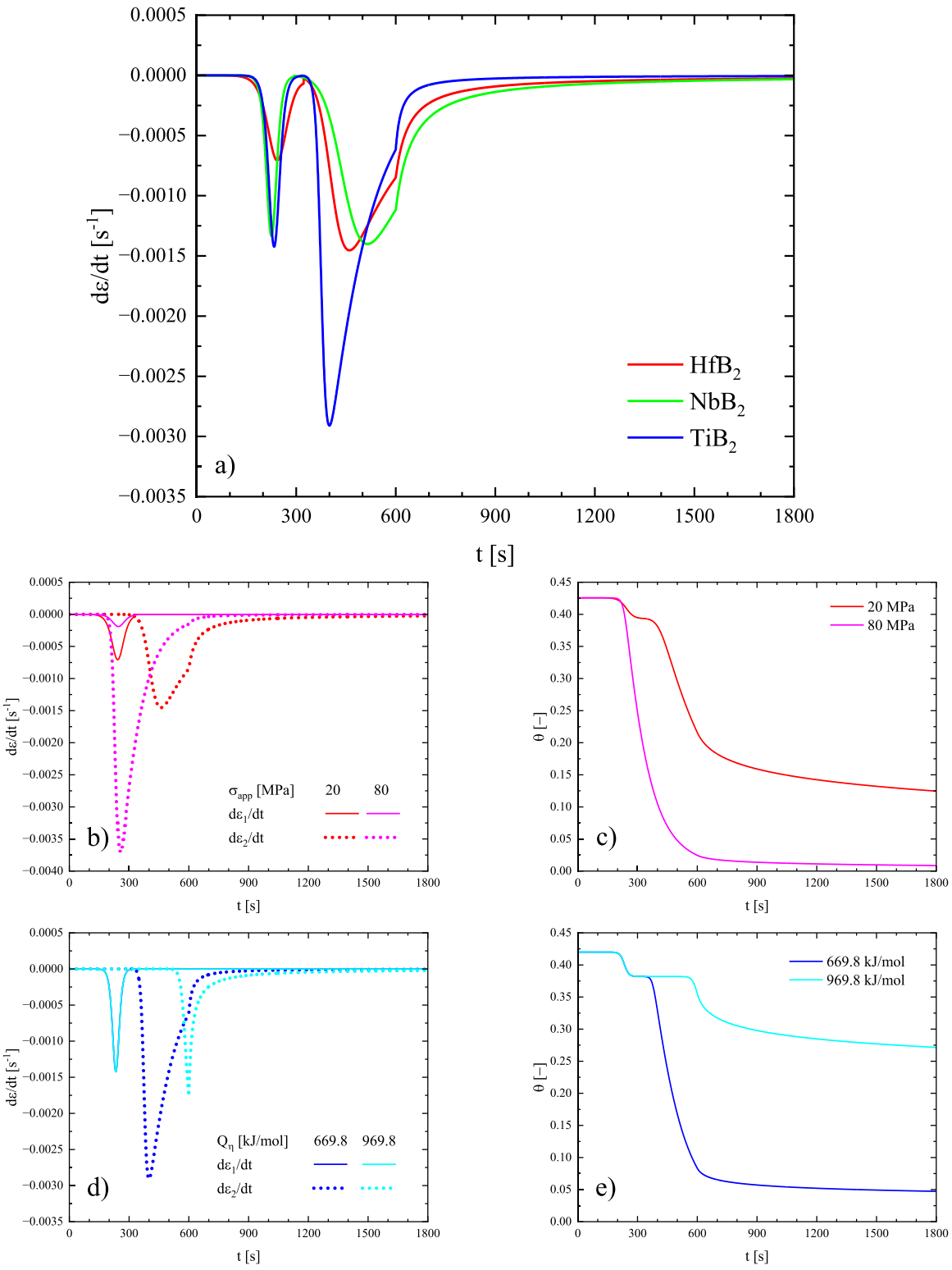

Fig. 5. a) Simulated strain rate during densification by SPS of transition metal diborides (σ_{app} = 20 MPa; t_H = 600 s; T_D = 1950 °C); b) effect of applied pressure on strain rates time evolution for HfB_2; c) effect of applied pressure on porosity time evolution for HfB_2; d) effect of shear viscosity activation energy on strain rates time evolution for TiB_2; e) effect of shear viscosity activation energy on porosity time evolution for TiB_2.

isothermal heating period. This behavior is consistent with its lower sensitivity exponent *m*, which results in a sharper switch between deformation regimes. In contrast, HfB_2 and NbB_2 show smoother strain rate transitions, with HfB_2 exhibiting slightly earlier and more gradual strain rate evolution than NbB_2. These results evidence the different rheological characteristics extracted from the model fits and provide insight into the time-dependent consolidation kinetics of each diboride system under identical external loading.

Fig. 5b shows the strain rate profiles of the two rheological components, slider ($\dot{\varepsilon}_1$) and dashpot ($\dot{\varepsilon}_2$), as functions of time during SPS of HfB_2, under two applied pressures: 20 MPa (solid and dotted red lines) and 80 MPa (solid and dotted magenta lines). The simulation isolates the

deformation contributions of each mechanism, providing insight into their relative timing of activation and interaction. At 20 MPa, the strain rate profile clearly shows a sequential activation of the involved mechanisms. The slider (solid red line) dominates the early densification occurring during the first period of heating (~150–300 s), corresponding to particle rearrangement under applied load. Once this mechanism is no longer operating and stress declines below the yield threshold, the dashpot (dotted red line) activates, driving densification through viscous deformation during the later heating period and dwell stage. This time separation confirms that, at lower pressure, particle rearrangement and viscous deformation occur primarily in series. In contrast, at 80 MPa, both slider and dashpot are active simultaneously during heating. The higher stress magnitude accelerates viscous deformation and reduces the temporal dominance of the slider. As a result, the characteristic peak in rearrangement strain rate is largely masked by the concurrent viscous response, which begins earlier and rises more sharply. This overlap of mechanisms demonstrates that, at higher applied pressures, the two deformation modes act in parallel, rather than sequentially. This analysis highlights that the apparent dominance and sequence of deformation mechanisms during SPS are not solely due to intrinsic material properties, but also strongly depend on the applied pressure. The model ability to resolve these contributions offers a powerful tool for optimizing processing conditions to favor desired densification pathways.

In Fig. 5c, the time evolutions of porosity θ corresponding to the same simulations reported in Fig. 5b are presented. It is clearly shown the effect of pressure on the kinetics and extent of consolidation. At 80 MPa, porosity decreases rapidly, and the sample nearly reaches full density ($\theta \sim 0.01$) within the first 600 s, even before the isothermal dwell stage begins. In contrast, at 20 MPa, the densification process is slower and remains incomplete, with porosity leveling off above 10 %.

An important result from Fig. 5c is that at high applied pressure, the contribution of particle rearrangement can be entirely masked within the densification curve. The apparent smooth, rapid densification may lead to the incorrect assumption that viscous sintering alone is responsible for the observed behavior. However, as shown in Fig. 5b, particle rearrangement is still active, but its strain signature becomes indistinguishable from the viscous contribution in the macroscopic porosity profile (cf. Fig. 5**c**). This illustrates a critical limitation in interpreting densification data using porosity-time curves alone. Without a mechanistic model that separates the deformation modes, the risk is to overestimate the role of viscous deformation and neglect early-stage rearrangement, leading to significant errors in the derivation of rheological parameters such as activation energy and viscosity pre-exponential factors (cf. Table 3).

While Fig. 5c highlights how the applied pressure influences the visibility and sequencing of the two densification mechanisms, the effect of material properties, specifically the activation energy for viscous flow, is shown in Fig. 5d. The latter presents the strain rate profiles of the slider ($\dot{\varepsilon}_1$) and dashpot ($\dot{\varepsilon}_2$) during SPS of TiB_2, simulated using two different values of activation energy for viscous flow, i.e., the reference value $Q_\eta = 669.8$ kJ/mol (dark blue curves) and an artificially increased value $Q_\eta = 969.8$ kJ/mol (cyan curves). This analysis isolates the effect of thermal activation on the relative timing of the two deformation mechanisms. For the reference Q_η, the transition from particle rearrangement (slider activity) to viscous deformation (dashpot activity) is nearly continuous. As the slider strain rate decays after ~300 s, the dashpot is already becoming active, creating an overlap between the mechanisms, similar to the low-pressure case for HfB_2 shown in Fig. 5b.

However, when the activation energy is increased to 969.8 kJ/mol, viscous flow is strongly suppressed during heating, and dashpot activation is significantly delayed, only emerging well after the completion of particle rearrangement. This introduces a temporal gap between mechanisms, in which neither slider nor dashpot are substantially active. The strain rate briefly falls toward zero before recovering during the dwell phase. This behavior contrasts with previous cases and demonstrates the possibility of a third mechanistic regime, where viscous deformation is delayed (Fig. 5d), in addition to the sequential, immediate transition (Fig. 5b, 20 MPa) and the simultaneous overlap (Fig. 5b, 80 MPa). These results emphasize that the relative timing of particle rearrangement and viscous deformation is not fixed but depends on a complex interplay between material parameters (e.g., viscosity) and operating conditions (e.g., pressure, heating rate). The proposed mechanistic model may help to reveal such distinctions, which are invisible in experimental porosity data alone.

For the sake of completeness, Fig. 5e shows the evolution of porosity θ corresponding to the simulation reported in Fig. 5d. For the reference value of Q_η, densification proceeds rapidly after the completion of particle rearrangement, reaching high density level during the early dwell period (dark blue curve). In contrast, with the increased activation energy, the delayed onset of viscous flow results in a slower porosity reduction and an incomplete densification even after 30 min. This finding implies that relatively high values of Q_η suppress viscous flow at intermediate temperatures, widening the temporal gap between the early-stage plastic response and the later-stage viscous consolidation.

The results presented in Fig. 5 collectively highlight the versatility and physical fidelity of the proposed rheological model. By explicitly capturing the time-dependent interaction between particle rearrangement and viscous deformation, the model reveals how densification mechanisms are influenced not only by material properties (e.g., activation energy, viscosity exponent) but also by external conditions such as applied pressure. Depending on these factors, deformation mechanisms may occur sequentially, overlap in time, or be separated by periods of mechanical inactivity. These insights, unresolvable from porosity curves alone, demonstrate the necessity of mechanistic modeling to guide accurate parameter identification and optimize sintering protocols for high-performance ceramics.

A potential concern with the proposed model could stem from the relatively high number of adjustable parameters (six), which might, in turn, raise the question of overfitting. In particular, one might argue that assuming a material linear behavior (i.e., $m = 1$) would reduce the parameter to four (cf. 2.2.3 and Table 3) and still allow for accurate reproduction of the experimental porosity profiles. However, attempts to optimize the model with $m = 1$ (not shown) did not satisfactorily succeed, indicating that the linear assumption fails to capture the densification behavior of all the investigated borides. To support this point, the isothermal stage (1950 °C), during which the slider is inactive since $\sigma_{eq} < \sigma_Y$ (cf. Fig. 4), is analyzed. The intrinsic material viscosity is calculated as the ratio between applied stress, σ_{app}, and equivalent strain rate, W, where the latter, which includes the effect of the varying porosity, has been evaluated from the (smoothed) experimental data reported in the inset of Fig. 6. As shown in this figure, the viscosity increases significantly with time, despite the constant temperature. This trend highlights the inherent strain-rate sensitivity of the viscous flow. Hence, a strain rate independent-viscosity model (i.e., $m = 1$) is inconsistent with experimental evidence in the case of TMBs densification, further justifying the inclusion of a non-Newtonian behavior in the model.

While the results discussed above clearly demonstrate that the linear case cannot reproduce the densification behavior of transition metal diborides under the investigated conditions, it is preferred to retain a generalized constitutive formulation capable of describing both Newtonian ($m = 1$) and non-Newtonian ($m \neq 1$) viscous behavior. This decision stems from the need for a flexible and broadly applicable framework. For different materials, temperatures, or other sintering regimes (e.g., viscous glass-forming ceramics), linear behavior may be a valid approximation. Hence, the model was developed with sufficient generality to allow such cases to emerge naturally from the parameter identification procedure, rather than imposing *a priori* any assumption. This approach ensures that the model can be extended or applied to a

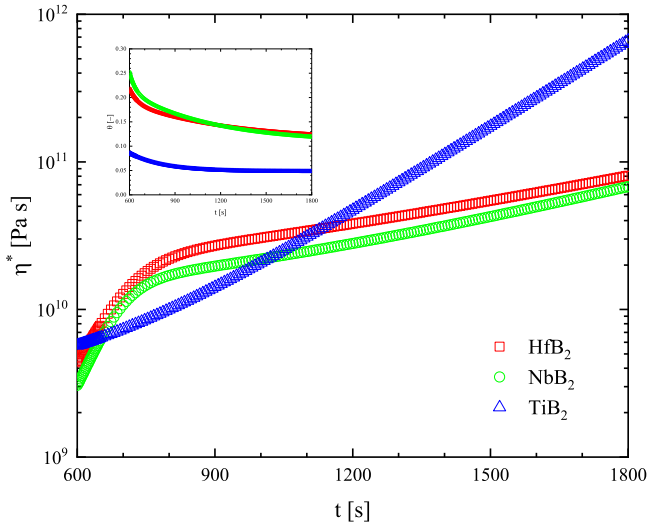

Fig. 6. Estimation of (porosity independent) shear viscosity η^* based on the experimental (smoothed) porosity time profiles during the isothermal period of densification reported in the inset.

wider class of materials or different consolidation methods without substantial modifications.

3.2. Apparent and intrinsic viscosity behavior during pressure-assisted sintering

This section investigates the rheological properties of HfB_2, NbB_2, and TiB_2 as modelled by means of the proposed approach, with a particular emphasis on the evolution of apparent and intrinsic viscosities, the role of strain-rate sensitivity, and the physical interpretation of fitted parameters such as the activation energy and the coefficient m. This analysis combines simulated and experimentally derived values to clarify how material response varies with temperature, strain rate, and porosity.

Fig. 7 displays the time evolution of the apparent viscosity μ during SPS of HfB_2 (red), NbB_2 (green), and TiB_2 (blue). A striking feature is the drastic initial decrease in viscosity, spanning more than 80 orders of magnitude within the first few hundred seconds. This sharp decrease is primarily governed by the rapid temperature rise during heating, which reduces both the shear viscosity, η, and bulk viscosity, κ. Closer inspection of the inset (300–600 s) reveals the presence of a viscosity minimum occurring before the end of the non-isothermal heating stage. Such a behavior reveals competing effects: on one hand, the continued increase in temperature tends to lower viscosity; on the other hand, the progressive loss of porosity (i.e., improved densification) increases mechanical resistance and tends to raise the viscosity. The presence of a minimum value thus reflects a crossover point where thermal softening is momentarily balanced by microstructural stiffening. After this point, the apparent viscosity increases slightly before stabilizing during the isothermal dwell stage.

Material-specific trends are also evident. TiB_2 exhibits the highest viscosity in the early stage, consistent with its greater stiffness and slower initial densification. However, due to its higher strain-rate sensitivity (lower m), TiB_2 undergoes a sharper drop in viscosity and rapidly transitions toward a more plastic-like response as shear rate increases. By the start of the dwell period, all three materials converge to similar viscosity levels, corresponding to fully activated viscoplastic flow at steady temperature and low strain rates. It is worth noting that the observed viscosity minimum, and the interplay between thermal softening and densification-induced stiffening, can only be observable through mechanistic modeling that resolves time-dependent porosity and strain rate contributions.

Fig. 8 shows the calculated zero-rate shear viscosity η^0 of dense HfB_2 (red), NbB_2 (green), and TiB_2 (blue) as a function of temperature. This property, which represents the intrinsic shear viscosity of each material (i.e., independent of porosity and strain rate), is obtained from the fitted parameters. All three borides exhibit the expected thermo-activated viscous response, with η^0 decreasing exponentially with increasing temperature, consistent with an Arrhenius-like trend. However, clear material-specific differences are evident. Specifically, TiB_2 shows the highest intrinsic viscosity across the temperature range, reflecting an inherently stronger resistance to thermally activated shear deformation. NbB_2 displays the lowest viscosity, indicating higher atomic mobility at lower temperatures, while HfB_2 lies between the two. It can be also seen that, at the process-relevant sintering temperatures ($T > 1500$ K), viscosity differences narrow but remain significant. For example, even at 2000 K, TiB_2 still exhibits a zero-shear viscosity several orders of magnitude higher than that of NbB_2.

This figure provides a useful benchmark for material comparison, offering insights into the intrinsic flow resistance that must be overcome during pressure-assisted densification. Importantly, these values cannot be extracted from porosity or strain data alone, because they are

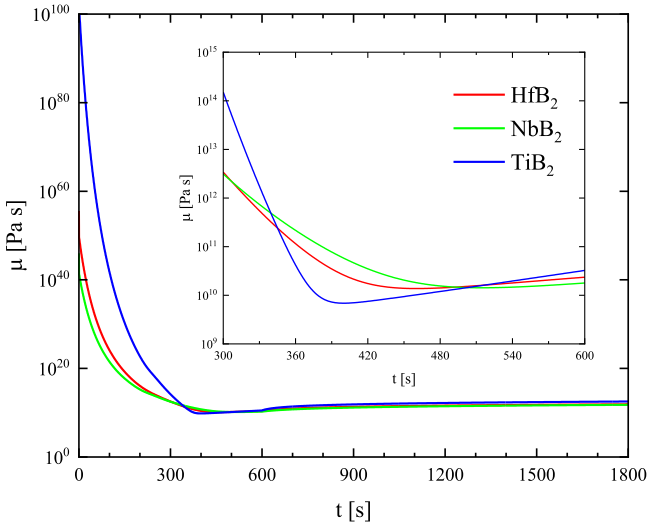

Fig. 7. Simulated apparent viscosity μ during densification of transition metal diborides ($\sigma_{app} = 20$ MPa; $t_H = 600$ s; $T_D = 1950$ °C).

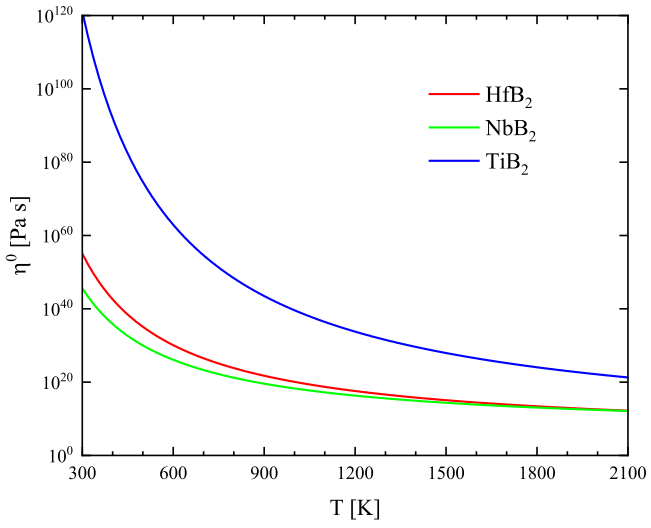

Fig. 8. Calculated zero-rate shear viscosity η^0 (porosity and strain-rate independent) of transition metal diborides as a function of temperature.

accessible only through the parameterized rheological modeling framework developed in this work. By isolating the viscosity temperature dependence from the porosity and strain rate ones, this analysis bridges the gap between experimental process response and fundamental material properties, thus providing a guide material selection and process tuning for applications requiring high-temperature formability or low flow resistance.

Although the model predicts extremely high apparent and zero-shear viscosity values at low temperatures (cf. Figs. 7 and 8), particularly below the active sintering range, this behavior is both expected and physically consistent with the adopted rheological framework. In fact, these values emerge from extrapolation to low temperatures of the viscosity description, which provides a mechanically consistent transition from the rigid solid-like behavior at low temperature and shear rate to the viscoplastic (fluid-like) flow under high temperature and shear rate. Importantly, although deformations corresponding to these high viscosities are hardly observable or experimentally measured, the proposed viscosity description is qualitatively validated by the negligible densification experimentally observed during the early heating stage (cf. Fig. 3).

Moreover, although the estimated viscosities at low temperatures may appear extremely high, such values are not only physically reasonable but have been known and accepted for decades within the ceramics and glass communities [35–37]. These high values reflect the inherent resistance of these materials to flow, particularly in the early stages of densification when deformation is strongly constrained by particle contacts and limited diffusion pathways. Overall, it should be emphasized that, beyond their exact numerical values, very high viscosity at low temperature serves primarily to limit deformation outside the range of operating conditions where densification is experimentally observed. In other words, they are essential for ensuring that the model simulates the transition from the rigid (undeformable)-body behavior to the fluid-like (densifying) one when temperature and applied pressure levels are increased.

Fig. 9 shows the simulated shear viscosity η^* of HfB_2 (red), NbB_2 (green), and TiB_2 (blue) as a function of the equivalent strain rate W at the constant temperature of 1950 °C. The curves correspond to model predictions based on the fitted parameters, while the discrete markers represent viscosity values indirectly estimated from the experimental porosity evolution during the isothermal dwell stage (cf. Fig. 6). All three materials exhibit clear non-Newtonian shear-thinning behavior,

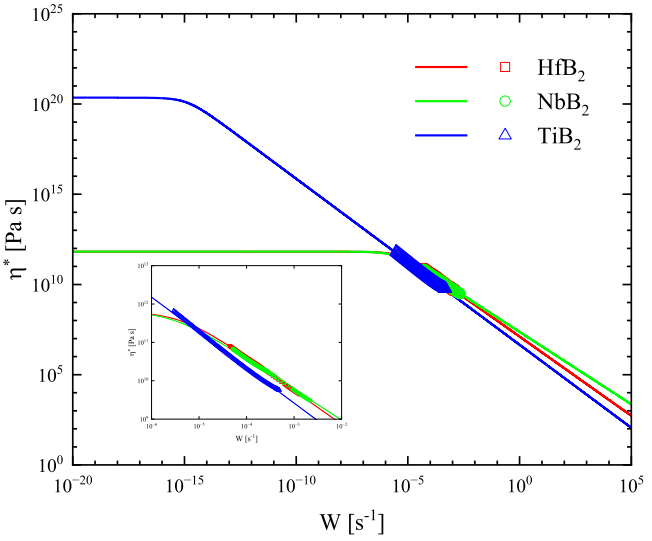

Fig. 9. Simulated (lines) of shear viscosity η^* of dense (pore less) transition metal diborides at 1950 °C as a function of the equivalent strain rate. Points represent the shear viscosity η^* at the same temperature as the estimate based on (smoothed) experimental data related to the isothermal period (cf. Fig. 6).

consistent with the adopted Bird–Carreau model. At very low strain rates, TiB_2 retains an extremely high viscosity plateau (as seen in Figs. 7 and 8), indicating a much more solid-like response in the low-deformation regime. In contrast, NbB_2 and HfB_2 transit into the shear-thinning region and reach comparable viscosities with TiB_2 at higher strain rates.

The experimental viscosity estimates (symbols) align closely with the predicted curves in the strain rate range covered by the SPS data, confirming the validity of the proposed model. The inset highlights this match on a magnified scale, further validating both the fitting methodology and the extracted rheological parameters. Together with Figs. 7 and 8, this analysis confirms that apparent viscosity during sintering results from the interaction of material intrinsic (bulk) viscosity, the evolving porosity, and the imposed shear rate. The zero-rate viscosity η^0 (Fig. 8) serves then as the upper limit of η^* as $W \to 0$.

While the sintering process under standard SPS conditions typically operates in the shear-thinning (non-Newtonian) regime due to elevated shear rates, realistic linear-viscous behavior is expected under specific conditions. Innately, at low external stresses (e.g., $\ll 20$ MPa), the strain rate induced during SPS is significantly low. If the material is also partially consolidated, the reduced driving force for densification can lead to near-zero effective strain rates, especially during the latter part of the dwell period. Under such conditions, the Bird–Carreau model naturally approaches its Newtonian plateau ($\eta^* \to \eta^0$).

Furthermore, in interrupted or slow-ramp sintering experiments, especially those designed to examine early-stage sintering or stress relaxation, densification proceeds very slowly [38,39]. These conditions are commonly used to study sintering kinetics or microstructure evolution at low driving forces and would naturally fall into the linear regime. In some alternative applications of the SPS process, sintering is carried out pressure-less, or the applied load is removed after an initial consolidation stage, while the temperature level is held, to retain the desired porosity [40,41]. In these cases, the still porous samples could then experience low strain rates so that sintering could occur in the Newtonian (linear-viscous) regime.

These examples demonstrate that the linear-viscous plateau predicted by the Bird–Carreau model is not only a formal extrapolation but corresponds to realistic thermomechanical conditions. Therefore, the use of a rheological model that allows for both linear and non-linear regimes, rather than enforcing a power-law creep formulation with $m < 1$, enhances the versatility of the proposed approach and expands upon classical sintering descriptions, such as those based on the conventional creep models.

Finally, it should be pointed out that the use of the Bird–Carreau constitutive law offers another significant advantage over classical power-law (Norton-type) formulations. As shown above, the Bird–Carreau model allows for the identification of the zero-shear viscosity η^0 which characterizes the intrinsic material resistance to deform in the limit of low strain rates. This information is inaccessible in traditional approaches, which inherently assume non-Newtonian behavior across all strain rates and do not represent a Newtonian plateau. As such, the Bird–Carreau formulation provides a more flexible and physically meaningful framework for capturing the full range of material rheology relevant to sintering.

3.3. Model validation using literature data and identification of optimal sintering conditions

Fig. 10 presents a validation of the rheological sintering model through a direct comparison with experimental data from the literature for HfB_2, NbB_2, and TiB_2. Each panel explores the model ability to capture the densification response under varying processing conditions and for the different materials. In Fig. 10a, the model successfully reproduces the trend of increasing final density of HfB_2 with dwell temperature, as reported by Venugopal et al. (2014) and Dubey et al. (2025)

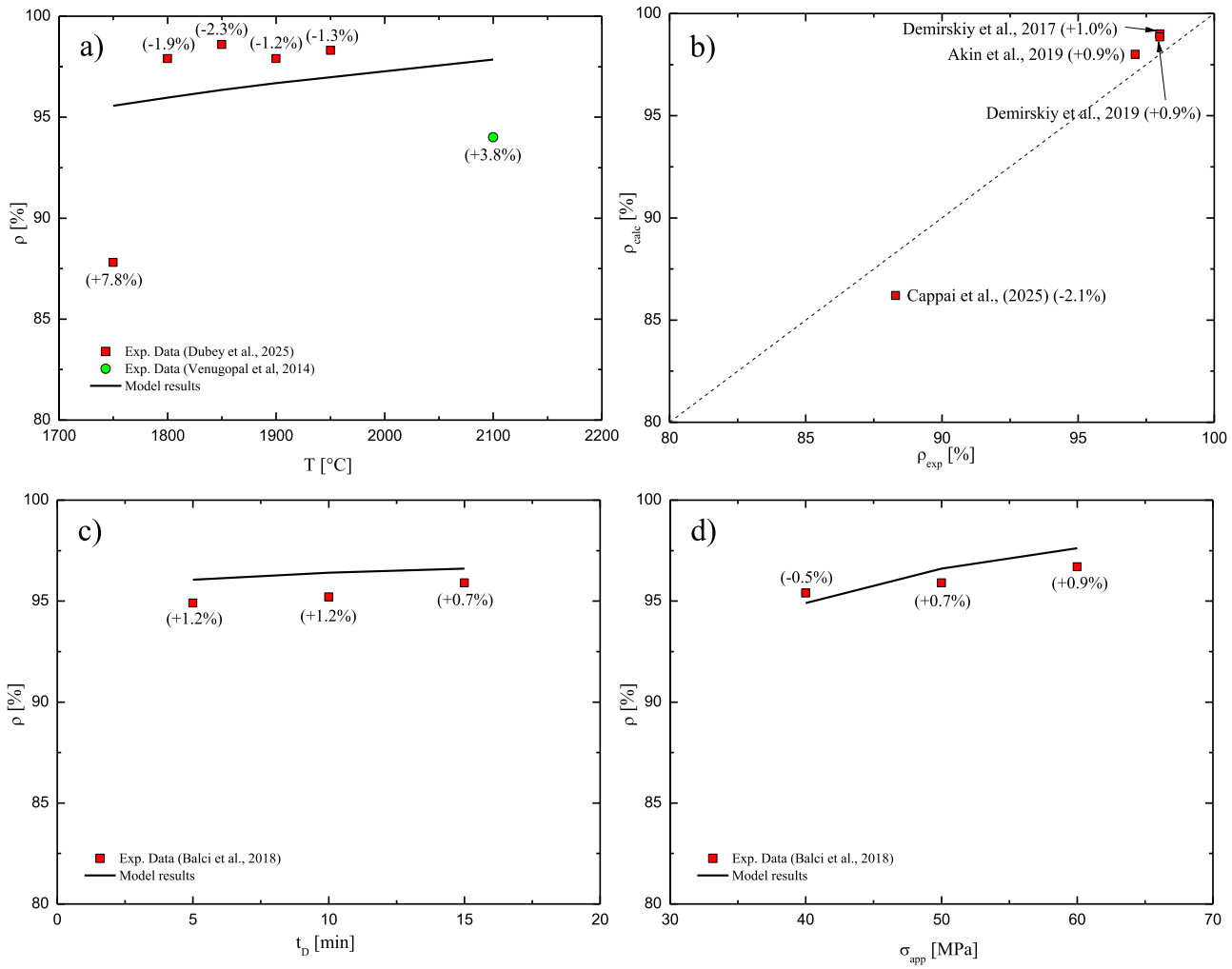

Fig. 10. Comparison between experimental data taken from the literature and model outcomes: a) final relative density of HfB_2 samples as a function of the dwell temperature, T_D ($HR = 100$ °C/min; $t_D = 10$ min; $\sigma_{app} = 50$ MPa) – data from Venugopal et al. (2014) [42] and Dubey et al. (2025) [43]; b) final calculated relative density of NbB_2 samples versus the experimental one. Operating conditions are as follows: Akin et al., 2019 [44]: $HR = 2$ °C/min; $T_D = 1750$ °C, $t_D = 5$ min, $\sigma_{app} = 50$ MPa; Cappai et al., 2025 [19]: $HR = 185$ °C/min; $T_D = 1850$ °C, $t_D = 20$ min, $\sigma_{app} = 20$ MPa; Demirskyi et al., 2017 [45]: $HR = 110$ °C/min; $T_D = 1950$ °C, $t_D = 10$ min, $\sigma_{app} = 80$ MPa; Demirskyi et al., 2019 [46]: $HR = 110$ °C/min; $T_D = 1900$ °C, $t_D = 10$ min, $\sigma_{app} = 80$ MPa; c) final relative density of TiB_2 samples as a function of the dwell time, t_D ($HR = 50$ °C/min; $T_D = 1500$ °C; $\sigma_{app} = 50$ MPa) – data from Balcı et al., 2018 [47]; d) final relative density of TiB_2 samples as a function of the applied pressure, σ_{app} ($HR = 50$ °C/min; $T_D = 1500$ °C; $t_D = 15$ min) – data from Balcı et al., 2018 [47]. Numbers in brackets indicate the difference (percentage) between the calculated and the experimental relative densities.

[42,43], using a constant heating rate (HR) of 100 °C/min, a dwell time of 10 min, and an applied pressure of 50 MPa. The deviations between predicted and measured densities remain within ±3.8 % (except for just a single datum), highlighting the accuracy of the proposed model across a broad temperature range.

Model-predicted and experimentally measured final densities for NbB_2 are compared in Fig. 10**b**, drawing from several sources with significantly different SPS parameters. Despite the variability in heating rates (ranging from 2 to 185 °C/min), dwell temperatures (1750–1950 °C), pressures (20–80 MPa), and dwell times (5–20 min), the model maintains good agreement, with differences below ±2.1 %. In Fig. 10**c**, the predicted evolution of TiB_2 density as a function of dwell time at 1500 °C and 50 MPa ($HR = 50$ °C/min) closely matches the experimental results from Balcı et al. (2018) [47]. The model captures the weak sensitivity of final density to extended dwell times in this material, which is consistent with the relatively high viscosity and low strain rate observed for TiB_2 after a significantly high degree of densification is already achieved. Finally, Fig. 10**d** shows the dependence of TiB_2 final density on applied pressure at fixed thermal conditions ($T_D = 1500$ °C, $t_D = 15$ min). The model predicts a clear increase in densification with increasing pressure, consistent with experimental observations. The maximum deviation remains below 1 %, confirming that the model robustly predicts the influence of pressure on the densification kinetics.

Collectively, these validation results demonstrate that the proposed rheological model, calibrated solely on experimental porosity-time data under a single set of SPS conditions, can be effectively extrapolated to a wide range of thermal and mechanical scenarios. This generalization capability is crucial for the predictive use of the model in process optimization and materials design. Overall, the consistency between predictions and literature data, despite differences in sintering setup, powder batches, and possible microstructural variability, validates the transferability and predictive strength of the rheological model when fitted using only a limited set of porosity-time data.

Along this line, Fig. 11 explores the densification response of transition metal diborides (HfB_2, NbB_2, TiB_2) under a range of SPS conditions, highlighting the model predictive capabilities and, crucially, revealing the relative effectiveness of different process variables in promoting full densification. Specifically, Fig. 11a presents the porosity evolution simulated over an extended processing time to 12 h at

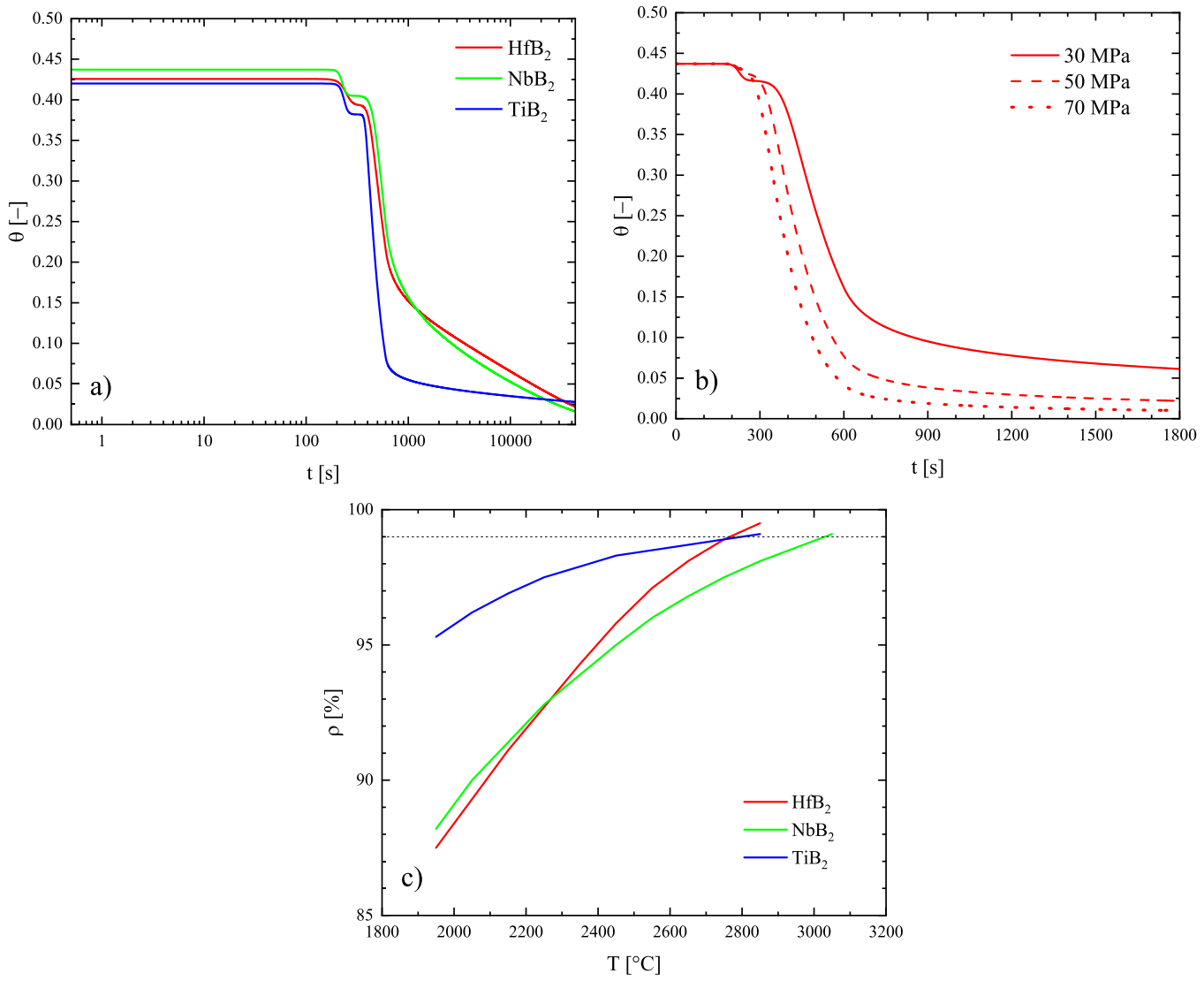

Fig. 11. Simulated effect of operating conditions on densification of transition metal diborides: a) porosity time profile up to 12 h (σ_{app} = 20 MPa; t_H = 600 s; T_D = 1950 °C); b) HfB_2 porosity time profile for different values of the applied pressure, σ_{app}; c) final relative density as function of the dwell temperature (σ_{app} = 20 MPa; t_H = 600 s; t_D = 1200 s). Dashed line in Figure c) gives the 99 % relative density.

constant temperature (1950 °C) and low applied pressure (20 MPa). Despite the prolonged holding time, none of the materials attain full density (defined here as relative density >99 %). This clearly indicates that under moderate pressure, densification eventually stalls due to insufficient driving force for viscous deformation and pore closure. Notably, TiB_2 densifies faster than HfB_2 and NbB_2, due to its higher strain rate sensitivity and despite its higher intrinsic viscosity (cf. Table 2 and Fig. 8), but still fails to cross the full density threshold within practical sintering times.

Fig. 11b directly confirms the conclusion that applied pressure is the most influential variable for achieving full density. At a fixed temperature and sintering time, increasing the pressure from 30 to 70 MPa significantly accelerates densification of HfB_2, with higher pressure yielding a denser final microstructure. The predicted final relative density as a function of the dwell temperature at constant pressure (20 MPa) and total sintering time (30 min) is illustrated in Fig. 11c for the three borides investigated in this work. While relative density increases with temperature, the thermal levels required to achieve > 99 % dense samples should exceed 2700 °C for all the investigated diborides. These temperature levels are experimentally challenging or nearly impractical for all conventional pressure-assisted sintering techniques, due to intrinsic limitations in equipment and risk of failures at such extreme temperatures.

Taken together, Fig. 11a–c indicate that while temperature and time are important, pressure seems to be the most effective and experimentally accessible variable for ensuring full densification of these ultra-high temperature borides. This conclusion is qualitatively supported by literature reports: for example, Sani et al. [48] demonstrated that TiB_2 samples with high relative density required applied pressures of 60 MPa. Conversely, Cappai et al. [19] showed that, when lower pressures are used, the addition of sintering aids (e.g., graphite) becomes necessary to promote densification. The proposed model thus offers not only quantitative insight into densification kinetics, but also clear guidance for process optimization under practical constraints.

4. Concluding remarks

A rheological model for pressure-assisted densification of transition metal diborides has been developed and validated using experimental data from spark plasma sintering of HfB_2, NbB_2, and TiB_2. The model is based on the mechanical analog of a slider in series with a dashpot, capturing two key mechanisms of densification: an early-stage particle

rearrangement with plastic character, and a high-temperature consolidating stage driven by non-linear viscoplastic deformation. The constitutive behavior of the dashpot is described using a Bird–Carreau-type function, allowing the strain-rate sensitivity to emerge from data rather than being imposed a priori. In contrast to traditional creep-based approaches, the present framework provides a novel, and thermodynamically consistent description that unifies multiple densification mechanisms within a single formulation, thereby offering a new tool for predictive modeling of transition metal diboride consolidation.

Model parameters, including shear and bulk viscosities, yield strength, activation energies, and the sensitivity coefficient m were obtained by fitting experimental porosity-time profiles. The model successfully captures the distinct densification behaviors of the three diborides, particularly the enhanced plasticity of TiB_2 at elevated temperatures and the similar response of HfB_2 and NbB_2. Simulated stresses and strain-rates time evolutions were analyzed in detail, revealing the synergic effects of particle rearrangement and viscous deformation, and highlighting the transition from sequential to simultaneous operation of these mechanisms, depending on processing conditions. The calculated material viscosities are consistent with values reported in the literature for high-temperature ceramics and glasses, and the strain-rate dependence is experimentally confirmed from isothermal-stage data.

Importantly, the model shows strong predictive capability beyond the fitting variable ranges. It accurately reproduces final densities reported in independent SPS studies and provides insight into the influence of process variables. Simulation outcomes indicate that applied pressure is the most effective parameter for achieving near-full density, whereas extended dwell time or elevated temperature alone may not be sufficient or practical. This study offers a robust, physically grounded modeling framework that captures the complex densification behavior of transition metal diborides under SPS conditions. Beyond fitting, the model provides mechanistic insight and predictive power, enabling informed design of processing strategies for ultra-high-temperature ceramics. Its general structure is adaptable to other material systems and sintering methods where linear or nonlinear viscous flow and early-stage plasticity coexist.

CRediT authorship contribution statement

Gabriele Traversari: Visualization, Validation, Software, Methodology, Investigation, Data curation. **Antonio Mario Locci:** Writing – review & editing, Writing – original draft, Supervision, Formal analysis, Data curation, Conceptualization. **Roberto Orrù:** Writing – review & editing, Supervision, Funding acquisition. **Giacomo Cao:** Writing – review & editing, Supervision, Project administration, Funding acquisition. **Michele Brun:** Writing – review & editing, Formal analysis, Conceptualization. **Alberto Cincotti:** Writing – review & editing, Supervision. **Luca Cappai:** Investigation. **Giorgio Carta:** Writing – review & editing, Formal analysis, Conceptualization. **Mariano Casu:** Investigation.

Funding

This work has been developed within the framework of the project eINS-Ecosystem of Innovation for Next Generation Sardinia (cod. ECS 00000038), funded by the Italian Ministry for Research and Education (MUR) under the National Recovery and Resilience Plan (PNRR)—MISSION 4 COMPONENT 2, “From research to business” INVESTMENT 1.5, “Creation and strengthening of Ecosystems of innovation” and construction of “Territorial R&D Leaders”. Italian Ministry also funded this research for Research and Education (MUR) under the National Recovery and Resilience Plan (NRRP), Mission 4, Component 2, Investment 1.1, Call for tender No. 104 published on 2.2.2022 by the Italian Ministry of University and Research (MUR), funded by the European Un-ion—NextGenerationEU—Project Title I-CREATE—Innovative Class of REfrAcTory ceramics for extreme Environments—CUP F53D23002020006—Grant Assignment Decree No. 104 adopted on 2 February 2022 by the Italian Ministry of Ministry of University and Research (MUR).

Declaration of Competing Interest

The authors declare that they have no known competing financial interests or personal relationships that could have appeared to influence the work reported in this paper.

Acknowledgements

One of the authors (Mariano Casu) performed his activity in the framework of the Ph.D. in Innovation Sciences and Technologies at the University of Cagliari, Italy.

Appendix A. Supporting information

Supplementary data associated with this article can be found in the online version at doi:10.1016/j.jeurceramsoc.2025.117860.

References

[1] J. Meng, H. Fang, H. Wang, Y. Wu, C. Wei, S. Li, X. Geng, X. Li, J. Zhang, G. Wen, P. Wang, Effects of refractory metal additives on diboride-based ultra-high temperature ceramics: a review, Int. J. Appl. Ceram. Technol. 20 (3) (2023) 1350–1370, https://doi.org/10.1111/ijac.14336.

[2] S. Bajpai, S. Dubey, T. Venkateswaran, S.S. Singh, K. Balani, An insight to wetting and joining of HfB_2 and ZrB_2 based ultra high temperature ceramics: a review (art. no), Chem. Eng. J. 495 (2024) 153387, https://doi.org/10.1016/j.cej.2024.153387.

[3] Z. Cao, J. Sun, K. Zhang, W. Ji, K. Cai, B. Li, B. Liu, C. Fan, Advances in bulk TiB_2-based composites: densification and toughening (art. no), Compos. Part A Appl. Sci. Manuf. 185 (2024) 108318, https://doi.org/10.1016/j.compositesa.2024.108318.

[4] R. Savino, L. Criscuolo, G.D. Di Martino, S. Mungiguerra, Aero-thermo-chemical characterization of ultra-high-temperature ceramics for aerospace applications, J. Eur. Ceram. Soc. 38 (8) (2018) 2937–2953, https://doi.org/10.1016/j.jeurceramsoc.2017.12.043.

[5] D. Sciti, L. Zoli, T. Reimer, A. Vinci, P. Galizia, A systematic approach for horizontal and vertical scale up of sintered Ultra-High temperature ceramic matrix composites for aerospace – advances and perspectives (art. no), Compos. Part B Eng. 234 (2022) 109709, https://doi.org/10.1016/j.compositesb.2022.109709.

[6] S.D. Oguntuyi, O.T. Johnson, M.B. Shongwe, Spark plasma sintering of ceramic matrix composite of ZrB_2 and TiB_2: microstructure, densification, and mechanical Properties—A review, Met. Mater. Int. 27 (2021) 2146–2159, https://doi.org/10.1007/s12540-020-00874-8.

[7] R. Orrù, R. Licheri, A.M. Locci, A. Cincotti, G. Cao, Consolidation/synthesis of materials by electric current activated/assisted sintering, Mater. Sci. Eng. R Rep. 63 (4-6) (2009) 127–287, https://doi.org/10.1016/j.mser.2008.09.003.

[8] Y. Le Godec, S. Le Floch, Recent developments of High-Pressure spark plasma sintering: an overview of current applications, challenges and future directions (art. no), Materials 16 (3) (2023) 997, https://doi.org/10.3390/ma16030997.

[9] B. Ratzker, M. Sokol, Exploring the capabilities of high-pressure spark plasma sintering (HPSPS): a review of materials processing and properties (art. no), Mater. Des. 233 (2023) 112238, https://doi.org/10.1016/j.matdes.2023.112238.

[10] A.M. Laptev, M. Bram, D. Garbiec, J. Räthel, A. van der Laan, Y. Beynet, J. Huber, M. Küster, M. Cologna, O. Guillon, Tooling in spark plasma sintering technology: design, optimization, and application (art. no), Adv. Eng. Mater. 26 (5) (2024) 2301391, https://doi.org/10.1002/adem.202301391.

[11] E.A. Olevsky, Theory of sintering: from discrete to continuum, Mater. Sci. Eng. R 23 (2) (1998) 41–100, https://doi.org/10.1016/S0927-796X(98)00009-6.

[12] E.A. Olevsky, V. Tikare, T. Garino, Multi-scale study of sintering: a review, J. Am. Ceram. Soc. 89 (6) (2006) 1914–1922, https://doi.org/10.1111/j.1551-2916.2006.01054.x.

[13] A. Van der Laan, R. Epherre, G. Chevallier, Y. Beynet, A. Weibel, C. Estournès, Fully coupled electrothermal and mechanical simulation of the production of complex shapes by spark plasma sintering, J. Eur. Ceram. Soc. 41 (7) (2021) 4252–4263, https://doi.org/10.1016/j.jeurceramsoc.2021.02.010.

[14] A. Van der Laan, R. Epherre, C. Estournès, Numerical approach for the determination of multi-mechanisms of the densification of TiAl by spark plasma sintering (art. no), Intermetallics 141 (2022) 107435, https://doi.org/10.1016/j.intermet.2021.107435.

[15] J.S. Diatta, C. Couder, C. Harnois, S. Marinel, C. Manière, Modeling spark plasma sintering of zirconia with prediction of final stage high densification rate (art. no), Mater. Lett. 337 (2023) 133930, https://doi.org/10.1016/j.matlet.2023.133930.

[16] C. Manière, J.S. Diatta, C. Harnois, C. Couder, C. Bilot, S. Marinel, Pressure assisted sintering stress exponent assessment methods: accuracy analysis and effect of sintering stress (art. no), Mech. Mater. 181 (2023) 104664, https://doi.org/10.1016/j.mechmat.2023.104664.

[17] B. McWilliams, J. Yu, A. Zavaliangos, Fully coupled thermal–electric-sintering simulation of electric field assisted sintering of net-shape compacts, J. Mater. Sci. 50 (2) (2014) 519–530, https://doi.org/10.1007/s10853-014-8463-1.
[18] Z. Trzaska, G. Bonnefont, G. Fantozzi, J.-P. Monchoux, Comparison of densification kinetics of a TiAl powder by spark plasma sintering and hot pressing, Acta Mater. 135 (2017) 1–13, https://doi.org/10.1016/j.actamat.2017.06.004.
[19] L. Cappai, M. Casu, A.M. Locci, G. Cao, S. Garroni, V. Cannillo, D. Bellucci, R. Orrù, From individual to equimolar binary transition metal diborides: the case of (Nb0.5M0.5)B2, M=Ti, hf (art. no), J. Eur. Ceram. Soc. 45 (8) (2025) 117277, https://doi.org/10.1016/j.jeurceramsoc.2025.117277.
[20] A. Cincotti, A.M. Locci, R. Orrù, G. Cao, Modeling of SPS apparatus: temperature, current and strain distribution with no powders, AIChE J. 53 (3) (2007) 703–719, https://doi.org/10.1002/aic.11102.
[21] Z. Sobotka, Rheology of materials and engineering structures, Elsevier, 1984.
[22] R. Hill, The mathematical theory of plasticity, Oxford at the Claredon Press, 1950.
[23] A. Mendelson, Plasticity: theory and application, The MacMillan Company, 1968.
[24] G. Aryanpour, S. Mashl, V. Warke, Elastoplastic-viscoplastic modeling of powder compaction: application to hot isostatic pressing, Powder Metall. 56 (1) (2013) 14–23, https://doi.org/10.1179/1743290112Y.0000000027.
[25] C. Van Nguyen, Y. Deng, A. Bezold, C. Broeckmann, A combined model to simulate the powder densification and shape changes during hot isostatic pressing, Comput. Methods Appl. Mech. Eng. 315 (2017) 302–315, https://doi.org/10.1016/j.cma.2016.10.033.
[26] C.P. Kohar, E. Martin, D.S. Connolly, S. Patil, N. Krutz, D. Wei, K. Inal, A new and efficient thermos-elasto-viscopastic numerical implementation for finite element simulations of powder metals: an application to hot isostatic pressing, Int. J. Mech. Sci. 155 (2019) 222–234, https://doi.org/10.1016/j.ijmecsci.2019.01.046.
[27] K.A. Kuhn, C.L. Downey, Deformation characteristics and plasticity theory of sintered powder materials, Int. J. Powder Metall. 7 (1) (1971) 15–25.
[28] R.J. Green, A plasticity theory for porous solids, Int. J. Mech. Sci. 14 (1972) 215–224, https://doi.org/10.1016/0020-7403(72)90063-X.
[29] M. Abouaf, J.L. Chenot, G. Raisson, P. Bauduin, Finite element simulation of hot isostatic pressing of metal powders, Int. J. Numer. Methods Eng. 25 (1988) 191–212, https://doi.org/10.1002/nme.1620250116.
[30] V.I. Arnol'd. Mathematical Methods of Classical Mechanics, 2ª ed., Springer, 1989.
[31] A. Benaarbia, J.P. Rouse, W. Sun, A thermodynamically-based viscoelastic-viscoplastic model for the high temperature cyclic behaviour of 9–12% cr steels, Int. J. Plast. 107 (2018) 100–121, https://doi.org/10.1016/j.ijplas.2018.03.015.
[32] R.B. Bird, R.C. Armstrong, O. Hassager, Dynamics of polymeric liquids, in: Fluid Mechanics, 2nd Ed., 1, Wiley-Interscience, 1987.
[33] A.M. Locci, R. Orrù, G. Cao, Modeling of electric current assisted sintering: an extended fluid-like approach for the description of powders rheological behavior, Chem. Eng. Res. Des. 154 (2020) 283–302, https://doi.org/10.1016/j.cherd.2019.12.001.
[34] P. Hendrickx, J. Milligan, M. Brochu, Consideration of particle rearrangement during the modeling of spark plasma densification of Al-Mg alloy powders, Scr. Mater. 102 (2015) 7–10, https://doi.org/10.1016/j.scriptamat.2015.01.003.
[35] J.K. Mackenzie, R. Shuttleworth, A phenomenological theory of sintering, art. no. 310, Proc. Phys. Soc. Sect. B 62 (12) (1949) 833–852, https://doi.org/10.1088/0370-1301/62/12/310.
[36] W.D. Kingery, M. Berg, Study of the initial stages of sintering solids by viscous flow, evaporation-condensation, and self-diffusion, J. Appl. Phys. 26 (10) (1955) 1205–1212, https://doi.org/10.1063/1.1721874.
[37] G.W. Scherer, Sintering of Low-Density glasses: I, theory, J. Am. Ceram. Soc. 60 (5-6) (1977) 236–239, https://doi.org/10.1111/j.1151-2916.1977.tb14114.x.
[38] X. Du, Z. Zhang, Y. Wang, J. Wang, W. Wang, H. Wang, Z. Fu, Hot-pressing kinetics and densification mechanisms of boron carbide, J. Am. Ceram. Soc. 98 (5) (2015) 1400–1406, https://doi.org/10.1111/jace.13483.
[39] R.N. Maksimov, V.A. Shitov, A.S. Yurovskikh, Effect of rate-controlled sintering on characteristics of hot isostatically pressed transparent Yb-doped Lu2O3 ceramics, Mater. Lett. 211 (2018) 208–211, https://doi.org/10.1016/j.matlet.2017.10.013.
[40] W.L. Bradbury, E.A. Olevsky, Production of SiC-C composites by free-pressureless spark plasma sintering (FPSPS), Scr. Mater. 63 (1) (2010) 77–80, https://doi.org/10.1016/j.scriptamat.2010.03.009.
[41] R. Yamanoglu, Pressureless spark plasma sintering: a perspective from conventional sintering to accelerated sintering without pressure, Powder Metall. Met. Ceram. 57 (9-10) (2019) 513–525, https://doi.org/10.1007/s11106-019-00010-1.
[42] S. Venugopal, A. Paul, B. Vaidhyanathan, J.G.P. Binner, A. Heaton, P.M. Brown, Synthesis and spark plasma sintering of sub-micron HfB_2: effect of various carbon sources, J. Eur. Ceram. Soc. 34 (6) (2014) 1471–1479, https://doi.org/10.1016/j.jeurceramsoc.2013.12.025.
[43] S. Dubey, P. Shiven, K. Balani, Intermediate and final stage sintering kinetics of spark plasma sintered hafnium diboride, Ceram. Int. 51 (12A) (2025) 15475–15482, https://doi.org/10.1016/j.ceramint.2025.01.384.
[44] I. Akin, B.C. Ocak, F. Sahin, G. Goller, Effects of SiC and SiC-GNP additions on the mechanical properties and oxidation behavior of NbB_2, J. Asian Ceram. Soc. 7 (2) (2019) 170–182, https://doi.org/10.1080/21870764.2019.1595929.
[45] D. Demirskyi, I. Solodkyi, T. Nishimura, Y. Sakka, O.O. Vasylkiv, High-temperature strength and plastic deformation behavior of niobium diboride consolidated by spark plasma sintering, J. Am. Ceram. Soc. 100 (11) (2017) 5295–5305, https://doi.org/10.1111/jace.15048.
[46] D. Demirskyi, I. Solodkyi, T. Nishimura, O.O. Vasylkiv, Fracture and property relationships in the double diboride ceramic composites by spark plasma sintering of TiB_2 and NbB_2, J. Am. Ceram. Soc. 102 (7) (2019) 4259–4271, https://doi.org/10.1111/jace.16276.
[47] O. Balcı, D. Ağaoğulları, F. Muhaffel, M.L. Öveçoğlu, H. Çimenoğlu, I. Duman, Effect of sintering techniques on the microstructure and mechanical properties of niobium borides, J. Eur. Ceram. Soc. 36 (13) (2018) 3113–3123, https://doi.org/10.1016/j.jeurceramsoc.2016.05.014.
[48] E. Sani, M. Meucci, L. Mercatelli, A. Balbo, C. Musa, R. Licheri, R. Orrù, G. Cao, Titanium diboride ceramics for solar thermal absorbers, Sol. Energy Mater. Sol. Cells 169 (2017) 313–319, https://doi.org/10.1016/j.solmat.2017.05.038.